Manuscript File

Click here to view linked References

Finite elements with embedded interphases for strain localization in quasi-brittle materials

Marianna Puccia[a], Antonino Spada[a], Giuseppe Giambanco[a]

[a]*Department of Engineering, University of Palermo, Viale delle Scienze, Ed. 8, 90128, Palermo, Italy*

Abstract

The paper presents a continuous-discontinuous numerical strategy for simulating localized failure in structures made of quasi-brittle materials using finite elements. The strategy is based on observing acting stresses scenarios, when a diffuse degradation is followed by high deformation bands localizing in certain regions of the structure. The numerical strategy should encompass both situations in accordance with the material's constitutive model. This objective is achieved by introducing a thin layer into a finite element at a certain level of the deformation process. In this study, the thin layer is modeled for the first time by an interphase mechanical device whose constitutive behavior is the same as the bulk material. This is possible since the interphase adds internal strains and stresses to the contact ones. As a consequence, no additional constitutive model and parameters are needed, unlike the zero-thickness interface or cohesive zone models commonly employed.
The proposed numerical strategy is illustrated in detail both at the element level and at the structural level. A new crack tracking algorithm has been developed based on decomposition of the model into substructures to allow cracks to cross arbitrary meshes. Some benchmark examples are presented showing the mesh-size and mesh-bias independence of results, together with the convergence behavior of the model.

Keywords: Localization, Interphase, Quasi-brittle materials, Isotropic Damage Model.

1. Introduction

During their softening stage, rate independent inelastic solids consisting of quasi-brittle materials exhibit strain localization in relatively narrow

zones. Narrow zones are characterized by the formation of micro-cracks and micro-voids whose evolution represents the macroscopic crack.

A number of researchers have been fascinated by the theoretical and computational aspects of this mechanical phenomenon. In the pioneering work of Rudnicki and Rice [1], later generalized by Ottosen and Runesson [2], the onset of localized deformations is triggered by the attainment of a critical stability condition at the constitutive level where discontinuous bifurcation of the strain state occurs.

The evolution of the localization band can be modeled using the discrete or the continuum approach.

In the discrete approach the localization band is depicted as a material volume confined by two surfaces, called *weak discontinuity surfaces*. Their distance or band thickness is generally considered constant and represents an additional constitutive parameter of the material. In the band the strain state can be decomposed in the *in plane* components and in the *out of plane* components, being the former regular and the latter discontinuous. This is known as *weak discontinuity* and can be captured by an apposite enrichment of the strain field [3, 4].

If the thickness of the band is small compared to the typical dimensions of the structure, the strain state can be assumed to be uniform throughout the thickness. It can be evaluated measuring the displacement of the surfaces delimiting the localization area. Adopting the zero thickness interface (ZTI) model the in plane strain components are neglected and the out of plane components are evaluated on the basis of the displacement jumps between the two weak discontinuity surfaces. In literature this kinematic description of the strain state of the band is known as *strong discontinuity* model [5, 6, 7].

The continuum modelling approach is mainly expressed in the formulation of advanced constitutive models as the non-local [8] and gradient models [9], where the response of a material point is related to its neighbours. In this case the strain discontinuity is regularized on the material volume, enriching the physical content of the local material models with one or more intrinsic length parameters. Consequently, the constitutive equations describe more accurately the real material behavior.

Most recently, the phase field theory has been applied to the problem of strain localization [10, 11] by introducing the phase variable to describe the smooth transition from the sound material to the localized material. In this sense, phase field models belong to the class of regularized continuum models.

From a computational point of view research efforts have been mostly concentrated on the simulation of the localization phenomenon, using the finite element method and adopting the discrete approach. In this field we can distinguish between studies where the strong discontinuity is *interelement* located and studies where it is *intraelement* located.

In the first case, the ZTIs are pre-defined between opposite sides of adjacent elements or the mesh is rearranged in order to have ZTIs between two elements [12]. The specific cracking pattern resulting from the applied load is a subset of the spider web depicted by the interface elements [13, 14]. Crack formation, branching and coalescing are guided by the interface constitutive law.

In the second case, different strategies have been used to extend the capabilities of classical finite elements to model intraelement displacement jumps. The Generalized-Finite Element Method (G-FEM) [15] and the Extended-Finite Element Method (X-FEM) [16] are examples of such numerical strategies. In both cases the approximation of the field variable is enriched making use of the Partition of Unity Method (PUM) which first appeared in the work of Babuška et al. [17]. The most significant advantage of these methods is modelling discontinuities and their development without requiring the definition of a new mesh. These methods only increase the number of degrees of freedom in the elements intersected by the crack. However, the numerical integration of elements crossed by a discontinuity requires a special treatment, which is different in the presence of different interpolation basis (triangles, quadrilaterals, etc.), for 2D or 3D cases [18]. Even though the additional degrees of freedom cause a small increase in the overall computational cost, the implementation itself is time-consuming.

The Phantom Node Method (PNM) has been derived from the work of Hansbo and Hansbo [19] and can be considered as a variant of the X-FEM [20, 21] since it reinterprets the approximation of the X-FEM displacement field by the superposition of the displacement fields of two overlapped finite elements. The advantage of PNM compared to X-FEM is that no discontinuous interpolation functions are required since each overlapping element furnishes the displacement field on one side of the crack.

A tracking algorithm based on the Virtual Element Method (VEM) has been recently proposed [22]. This method introduces cohesive interfaces between polygons characterized by any number of edges. The ease of implementation, the absence of a parent element, and the high performance even in the presence of distorted elements or non-conforming meshes are the main ad-

vantages of the method. The main disadvantages are the need to insert new nodes or move some of the existing ones, and the difficulty of handling crack branching.

Self-propagating non-continuous crack models have been proposed in the framework of meshless method [23] or finite element method [24].

The Augmented Finite Element Method (A-FEM) [25, 26, 27, 28] operates at the element level and does not require enrichment of the shape functions to approximate the displacement field. In a different manner with respect to the PNM, A-FEM simulates weak and strong discontinuities by splitting the element into two mathematically separable standard elements which are adjacent to the discontinuity surface. Initially, additional degrees of freedom are introduced to decompose the cracked element. Then, they are condensed at the element equilibrium level. Hence, they are not present at the global level.

Some of the benefits of A-FEM are [25, 26, 27, 28]:

- elements are split into standard finite elements, fully compatible with standard finite elements packages;
- possibility to consider different material properties for the sub-elements;
- no need for level-set information or to necessarily know if a sub-element is below or above the discontinuity;
- reduced computational cost;
- straightforward implementation to 3D cases.

The principal difference of our approach with the classical A-FEM and X-FEM regards the possibility to follow the material failure from the strain localization in a thin layer band to the crack opening by using the interphase concept in place of the quite common ZTI model. The IPH was introduced by Giambanco and Mróz [29] and implemented in the finite element framework by Giambanco et al. [30]. The IPH model can be considered the enrichment of the ZTI since it allows to model both the contact and the internal strains of the thin layer. In addition, it extends the calculation of stresses also to internal components. As a consequence, the thin layer response is more realistic and some phenomena such as the squeezing effect can be captured [30]. The most relevant point is that, unlike ZTI models, IPH does not require a specific traction-displacement jump constitutive law and the constitutive

laws adopted for IPH can correspond to those of bulk material.
Additional efforts have been made to formulate an original crack tracking algorithm. The model is decomposed into non-localized elements and substructures where elements intersected by cracks are grouped.
The localization analysis is performed for a strain softening homogeneous continuum obeying the damage model with strain-based loading functions formulated by Jirásek [31]. However, the proposed numerical approach has general applicability and any constitutive model could be implemented. At the material point, the damage level is linked to a scalar variable representing the highest strain ever recorded during loading history. The localization band arises at the material point where the constitutive instability is detected but, according to the Delayed Embedded Crack (DEC) model [32, 33], the IPH is inserted upon stabilization of the band direction.
The band direction is identified through a spectral analysis of a fracture tensor introduced in this study. Convergence and validation of the model are assessed through benchmark examples and comparisons with experimental and numerical data available in the literature.
The paper is organized as follows. Section 2 shows the basic assumptions and derives the equilibrium equations for an IPH element. It also reports the fundamentals of the adopted constitutive model. In Section 3 and Section 4 details about the implementation at the finite element and structural levels respectively are reported, with particular attention to the crack tracking algorithm. Section 5 gathers the results of four different applications, while Section 6 gives the main conclusions of this work.

2. Problem definition

The mechanical problem regards a solid body Ω (Fig. 1), defined in the Euclidean space R^3, referred to the orthonormal frame $(0, \mathbf{e}_x, \mathbf{e}_y, \mathbf{e}_z)$. The body is constituted by a strain softening material, which under severe loading conditions presents a narrow zone Ω_b where strains concentrate. The body is subjected to volume forces $\mathbf{f}$, to tractions $\mathbf{t}$ on Γ_t and to kinematic constraints $\mathbf{u} = \overline{\mathbf{u}}$ on Γ_u respectively.
The thin material layer Ω_b has thickness w_b and is separated from the remaining parts Ω^+ and Ω^- by the weak discontinuity surfaces Σ^+, Σ^- where the displacement field is continuous and its gradient suffers discontinuity.
It is assumed that the band thickness is small if compared with the characteristic dimensions of the body and is modelled using an IPH model. Typical

of IPH or ZTI models, the band is also assumed to be locally planar. This means that any mechanical quantity related to band curvature is neglected. With these hypotheses at hand, in order to study the static and kinematic conditions of the localization band we refer to a local Cartesian coordinate system (x_b, y_b, z_b) with x_b, y_b axes lying within the middle plane Σ_b of the joint and the z_b axis coinciding with the normal unit vector $\mathbf{n}_b$ directed towards the body Ω^+, Figure 2. The thin layer is subject to the external tractions $\mathbf{t}$ on the lateral surface Γ_b and to the contact tractions $\mathbf{q}^+$ and $\mathbf{q}^-$ on the physical surfaces Σ^+ and Σ^-, respectively.

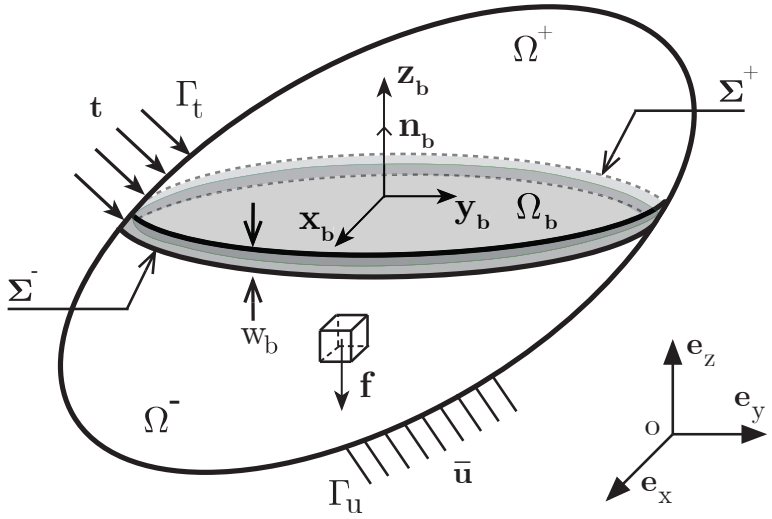

Figure 1: Schematic representation of a continuous body with a localization band.

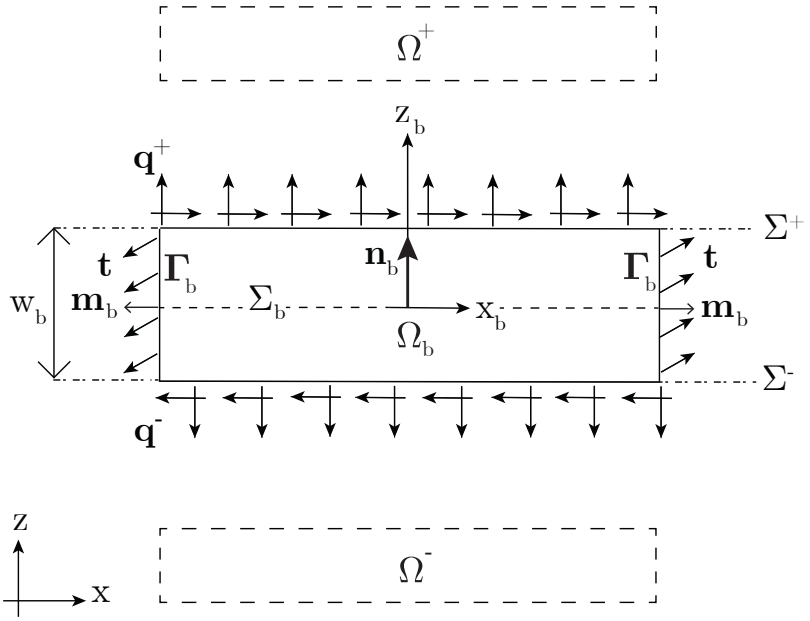

Figure 2: Schematic representation of the band volume.

2.1. Geometry and Kinematics

The geometric and kinematic assumptions for the localization band are:

- the localization band is planar;
- fibers in the z_b direction are maintained rectilinear along the deformation process;
- the band thickness w_b is small if compared to the characteristic dimensions of the solid;
- the strain state is uniform along the band thickness and is obviously equal to the average value along the same direction.

In view of the second hypothesis the displacement field $\mathbf{u}_b$ in the band can be easily obtained from the displacements $\mathbf{u}_b^+$, $\mathbf{u}_b^-$ in Σ^+ and Σ^-, thus

$$\mathbf{u}_b\left(x_b, y_b, z_b\right) = \left(\frac{1}{2} + \frac{z_b}{w_b}\right)\mathbf{u}_b^+\left(x_b, y_b\right) + \left(\frac{1}{2} - \frac{z_b}{w_b}\right)\mathbf{u}_b^-\left(x_b, y_b\right). \qquad (1)$$

Due to other hypotheses, the thin layer representing the localization band collapses in its middle surface Σ_b and the strain state can be calculated from Eq. (1) in the following way

$$\boldsymbol{\varepsilon}_b = \frac{1}{w_b} \int_{\frac{-w_b}{2}}^{\frac{w_b}{2}} \nabla^s \mathbf{u}_b \, \mathrm{d}z_b = \frac{1}{w_b} \left([\mathbf{u}_b] \otimes \mathbf{n}_b \right)^s + \nabla^s \hat{\mathbf{u}}_b \tag{2}$$

where $(\cdot \otimes \cdot)^s$ is the symmetric part of the resulting tensor, $\mathbf{n}_b$ is the unit vector normal to the middle surface of the localization band, ∇^s is the symmetric part of the gradient operator and

$$[\mathbf{u}_b] = \mathbf{u}_b^+ - \mathbf{u}_b^-, \qquad \hat{\mathbf{u}}_b = \left(\frac{\mathbf{u}_b^+ + \mathbf{u}_b^-}{2} \right). \tag{3}$$

Let us note that the joint curvatures generated by the displacement field (1) and the related flexural effects are neglected. Therefore, the strain state of the IPH depends on the displacement discontinuity $[\mathbf{u}_b]$ between the surfaces Σ^+ and Σ^- and on the displacements $\hat{\mathbf{u}}_b$ of the middle plane Σ_b of the localization band. Eq. (2) illustrates the decomposition of the total strain in two parts: the first term is the contact or irregular part $\boldsymbol{\varepsilon}_b^c$ while the latter is the internal or regular part $\boldsymbol{\varepsilon}_b^i$.

2.2. Forces and Equilibrium

Let us consider the IPH subject to the contact tractions $\mathbf{q}^+$ on the surface Σ^+, $\mathbf{q}^-$ on the surface Σ^- and to the external load $\mathbf{t}$ on the solid boundary Γ_b. The principle of virtual displacements (PVD) asserts that the work produced by the contact tractions and the external loads must be equal to the internal work developed in the localization band, thus

$$\int_{\Sigma^+} \delta \mathbf{u}_b^+ \cdot \mathbf{q}^+ \, \mathrm{d}\Sigma + \int_{\Sigma^-} \delta \mathbf{u}_b^- \cdot \mathbf{q}^- \, \mathrm{d}\Sigma + \int_{\Gamma_b} \delta \mathbf{u}_b \cdot \mathbf{t} \, \mathrm{d}\Gamma = \int_{\Omega_b} \delta \boldsymbol{\varepsilon}_b : \boldsymbol{\sigma}_b \, \mathrm{d}\Omega. \tag{4}$$

Virtual displacements, preceded by the symbol δ, are assigned while the virtual strains must satisfy Eq. (2). Since the strain state is uniform along the band thickness, consistently the stress state can also be considered uniform along the same direction. Therefore the internal work assumes the following expression:

$$\int_{\Omega_b} \delta\boldsymbol{\varepsilon}_b : \boldsymbol{\sigma}_b \, \mathrm{d}\Omega = \int_{\Sigma_b} [(\delta\,[\mathbf{u}_b] \otimes \mathbf{n}_b)^s + w_b \nabla^s \delta\hat{\mathbf{u}}_b] : \boldsymbol{\sigma}_b \, \mathrm{d}\Sigma \tag{5}$$

196 which applying the divergence theorem to the second term of the right-
197 hand side becomes

$$\int_{\Omega_b} \delta\boldsymbol{\varepsilon}_b : \boldsymbol{\sigma}_b \, \mathrm{d}\Omega = \int_{\Sigma_b} [(\delta\,[\mathbf{u}_b] \otimes \mathbf{n}_b)^s : \boldsymbol{\sigma}_b - w_b \, \delta\hat{\mathbf{u}}_b \cdot \mathrm{div}\boldsymbol{\sigma}_b] \, \mathrm{d}\Sigma + w_b \int_{C_b} \delta\hat{\mathbf{u}}_b \cdot (\boldsymbol{\sigma}_b \cdot \mathbf{m}_b) \, \mathrm{d}C. \tag{6}$$

198 C_b is the contour of the localization band middle surface and $\mathbf{m}_b$ is the
199 unit vector normal to the contour line.
200 Substituting the integral (6) in the PVD and assuming that $\Sigma^+ \equiv \Sigma^- \equiv \Sigma_b$,
201 using positions (3) and considering that the surface forces on Γ_b are uniform
202 along the thickness of the thin layer, we have

$$\int_{\Sigma_b} \delta\mathbf{u}_b^+ \cdot \left(\mathbf{q}^+ + \frac{w^b}{2} \mathrm{div}\boldsymbol{\sigma}_b - \boldsymbol{\sigma}_b \cdot \mathbf{n_b} \right) \mathrm{d}\Sigma + \int_{\Sigma_b} \delta\mathbf{u}_b^- \cdot \left(\mathbf{q}^- + \frac{w^b}{2} \mathrm{div}\boldsymbol{\sigma}_b + \boldsymbol{\sigma}_b \cdot \mathbf{n_b} \right) \mathrm{d}\Sigma + \int_{C_b} \delta\hat{\mathbf{u}}_b \cdot (\mathbf{t} - \boldsymbol{\sigma}_b \cdot \mathbf{m}_b) \, \mathrm{d}C = 0. \tag{7}$$

203 Since Cauchy's Theorem permits to write $\mathbf{q}^+ = \boldsymbol{\sigma}^+ \cdot \mathbf{n}_b$ and $\mathbf{q}^- = -\boldsymbol{\sigma}^- \cdot \mathbf{n}_b$
204 and (7) is valid for any virtual displacements $\delta\mathbf{u}^+$ and $\delta\mathbf{u}^-$, we finally obtain
205 the equilibrium equations of the IPH:

$$w_b \, \mathrm{div}\boldsymbol{\sigma}_b + [\boldsymbol{\sigma}_b] \cdot \mathbf{n_b} = \mathbf{0} \quad \text{on } \Sigma_b, \tag{8}$$

$$(\boldsymbol{\sigma}_b - \hat{\boldsymbol{\sigma}}_b) \cdot \mathbf{n_b} = \mathbf{0} \quad \text{on } \Sigma_b, \tag{9}$$

$$\boldsymbol{\sigma}_b \cdot \mathbf{m}_b = \mathbf{t} \quad \text{in } C_b, \tag{10}$$

206 where

$$[\boldsymbol{\sigma}_b] = \boldsymbol{\sigma}_b^+ - \boldsymbol{\sigma}_b^-, \qquad \hat{\boldsymbol{\sigma}}_b = \frac{\boldsymbol{\sigma}_b^+ + \boldsymbol{\sigma}_b^-}{2}. \tag{11}$$

207 Eqs. (8) and (9) can be regarded as internal and external equilibrium

equations of the IPH and (10) represents the equilibrium boundary conditions.
In the circumstance that the same constitutive behavior of the bulk material is used for the IPH, w_b represents the only additional parameter to be provided in order to solve Equation (8). It is relevant to note that w_b is a parameter that needs to be specified in any model where the band is assumed to collapse in its middle plane. This is the case with IPH or ZTI models.

2.3. Constitutive Model

The proposed computational procedure allows the implementation of any constitutive model involving localization bands. The choice of a specific constitutive model is strictly related to the material to simulate.
The numerical examples herein presented are developed with the well-known isotropic damage model with a strain-based loading function reported in [31]. In this simple model the stiffness moduli decrease proportionally in every direction and independently of loading direction, on the basis of the value assumed by the damage variable $D \in [0, 1]$. Consequently, the damaged secant stiffness tensor is expressed as

$$\mathbf{E_s} = (1 - D)\mathbf{E} \tag{12}$$

and the stress-strain relation can be written in the form

$$\boldsymbol{\sigma} = \mathbf{E_s}\,\boldsymbol{\varepsilon} = (1 - D)\,\mathbf{E}\,\boldsymbol{\varepsilon} \tag{13}$$

where $\mathbf{E}$ is the elastic stiffness tensor.
The evolution of damage depends on the internal kinematic variable κ. This variable is equal to the maximum value ever reached by the *equivalent strain* $\tilde{\varepsilon}$ along the loading path, i.e. a scalar measure of the strain level.
The elastic domain and the loading-unloading conditions are defined by the following damage activation function and related Kuhn-Tucker conditions:

$$f(\tilde{\varepsilon}, \kappa) = \tilde{\varepsilon} - \kappa, \tag{14}$$

$$f(\tilde{\varepsilon}, \kappa) \leq 0, \quad \dot{\kappa} \geq 0, \quad \dot{\kappa}\, f(\tilde{\varepsilon}, \kappa) = 0. \tag{15}$$

A different behavior in tension and compression is typical for quasi-brittle materials. Microcraks mostly grow when the material is stretched and it

is natural to consider this fact in the definition of the equivalent strain. Therefore, the so-called *Mazars* definition of the equivalent strain is adopted:

$$\tilde{\varepsilon} = \sqrt{\sum_{I=1}^{3} \langle \varepsilon_I \rangle^2} \tag{16}$$

where ε_I (I=1,2,3) are the principal strains and the McAuley brackets $\langle \cdot \rangle$ denote the positive part.

With the previous definition of the equivalent strain the evolution of the damage variable can be defined in the following way

$$D = g(\kappa) = \begin{cases} 0 & \text{if } \kappa \leq \varepsilon_0 \\ 1 - \frac{\varepsilon_0}{\kappa} \exp(-\frac{\kappa - \varepsilon_0}{\varepsilon_f - \varepsilon_0}) & \text{if } \kappa > \varepsilon_0 \end{cases}, \tag{17}$$

being ε_0 and ε_f the elastic and post-elastic limit strains, respectively.

3. Numerical procedure at the finite element level

The solution of a structure subjected to external actions where strains concentrate in a narrow band is now implemented in the framework of the finite element method. The fundamental relations are here numerically treated for a quadrilateral 2D element and an efficient procedure that exploits the A-FEM idea [25] is presented. The extension to meshes constituted of triangular 2D elements or generic 3D elements is straightforward since it involves the same fundamental relations. It is important to highlight that, within each element, the crack can only be straight in the present formulation. Variations in the crack direction and crack branching inside the element will be included in future developments.

Stress and strain states are written using Voigt's notation.

3.1. Intraelement band

Let us suppose that the finite element is crossed by a planar localization band identifying the two parts Ω^+ and Ω^- of the quadrilateral element (Fig. 3). Depending on the position and orientation of the localization band, the quadrilateral element can be split into two quadrilaterals (Fig. 3-a) or into a triangular and a pentagonal (Fig. 3-b) sub-element.

For the 2D problem the band is represented by the line Σ_b passing through point (x_{bp}, z_{bp}) and having the direction corresponding to the unit vector $\mathbf{n}_b$

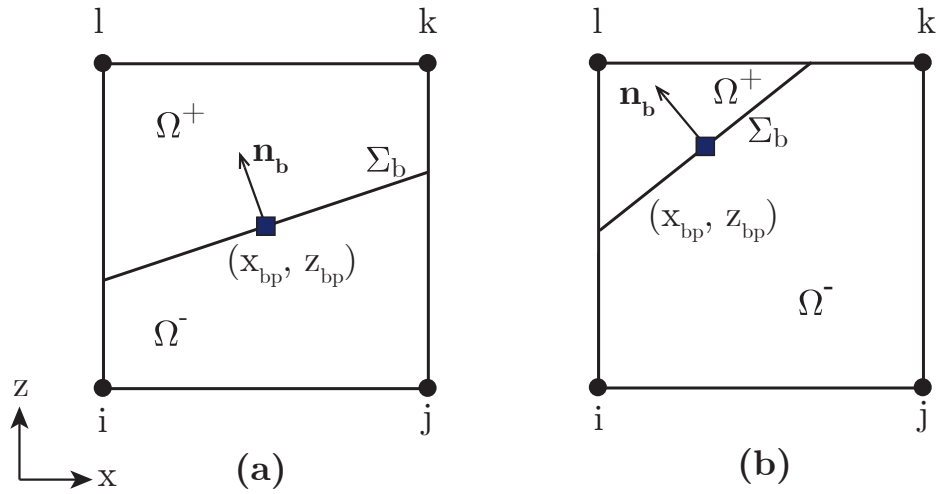

Figure 3: Four noded finite element crossed by the localization band: two quadrilateral sub-elements (a) and a triangular and a pentagonal sub-elements (b) cases.

pointing to the sub-domain Ω^+.
According to the A-FEM procedure the element Ω is replaced by the two sub-elements Ω^+ and Ω^- with degrees of freedom $\mathbf{U}^+$ and $\mathbf{U}^-$, respectively (Fig. 4). In the case of a pentagonal sub-element, this is considered as the assembly of three triangles as for Ω^- in Figure (4b). The interphase element Ω_b is embedded between the two elements by adding four additional nodes (m, n, r, s) which provide the degrees of freedom $\mathbf{U}_b$ of the interphase.
The subdivisions shown in Figure (4) hold for a 4-node quadrilateral element with bi-linear shape functions, which are the easiest numerical assumptions used as a first attempt in this work. In the presence of higher-order shape functions, in quadrilateral elements with more than 4 nodes, Ω^+ and Ω^- would each be subdivided into triangles, while for the interphase element six nodes are used, instead of four.

Considering the classical isoparametric formulation of quadrilateral finite elements, displacement and strain fields are derived from nodal displacements

$$\mathbf{u}^{(-,+)} = \mathbf{N}\,\mathbf{U}^{(-,+)}, \quad \boldsymbol{\varepsilon}^{(-,+)} = \mathbf{C}\,\mathbf{N}\,\mathbf{U}^{(-,+)} = \mathbf{B}\,\mathbf{U}^{(-,+)} \tag{18}$$

where $\mathbf{N}$ is the shape functions matrix and $\mathbf{C}$ is the kinematic compatibility matrix for plane problems.

The PVD for the two finite elements Ω^+ and Ω^- reads

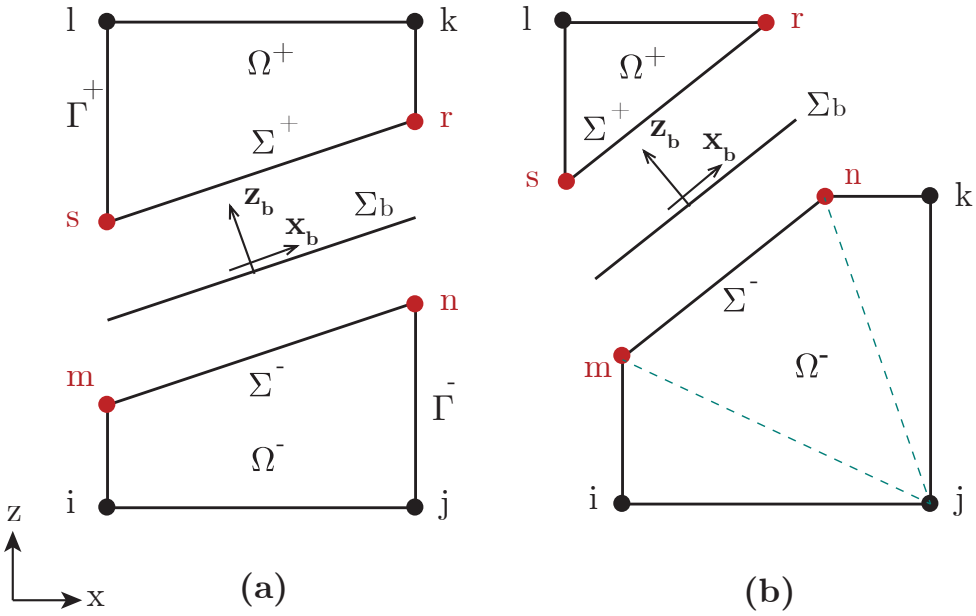

Figure 4: Sub-elements and additional nodes: two quadrilateral sub-elements (a) and a triangular and a pentagonal sub-elements (b) cases.

$$\delta\mathbf{U}^{(-,+)T}\left(\int_{\Omega^{(-,+)}}\mathbf{N}^T\mathbf{f}\,\mathrm{d}\Omega+\int_{\Gamma^{(-,+)}}\mathbf{N}^T\mathbf{t}^{(-,+)}\mathrm{d}\Gamma+\int_{\Sigma^{(-,+)}}\mathbf{N}^T\mathbf{q}^{(-,+)}\mathrm{d}\Sigma-\int_{\Omega^{(-,+)}}\mathbf{B}^T\boldsymbol{\sigma}^{(-,+)}\mathrm{d}\Omega\right)=0. \quad (19)$$

Solving the integrals by using the Gauss quadrature rule and considering that the equality (19) is valid for any virtual displacement field, we obtain the equilibrium equations of the two sub-elements:

$$\mathbf{F}_e^{(-,+)}+\mathbf{F}_i^{(-,+)}=\mathbf{K}^{(-,+)}\mathbf{U}^{(-,+)}, \quad (20)$$

where

$$\mathbf{F}_e^{(-,+)} = \int_{\Omega^{(-,+)}} \mathbf{N}^T \mathbf{f} \, \mathrm{d}\Omega + \int_{\Gamma^{(-,+)}} \mathbf{N}^T \mathbf{t}^{(-,+)} \mathrm{d}\Gamma \tag{21}$$

$$\mathbf{F}_i^{(-,+)} = \int_{\Sigma^{(-,+)}} \mathbf{N}^T \mathbf{q}^{(-,+)} \mathrm{d}\Sigma \tag{22}$$

$$\mathbf{K}^{(-,+)} = \int_{\Omega^{(-,+)}} \mathbf{B}^T \mathbf{E}_t \, \mathbf{B} \, \mathrm{d}\Omega. \tag{23}$$

$\mathbf{F}_e$ represents the nodal force array originated by external forces and tractions. $\mathbf{F}_i$ contains the nodal internal forces originated by tractions due to the discontinuity. $\mathbf{K}$ is the element tangent stiffness matrix, dependent on the elastic tangent operator $\mathbf{E}_t$.

Let us recall the stress-strain relation (13). $\mathbf{E}_t$ is defined as:

$$\boldsymbol{E_t} = \frac{\partial \boldsymbol{\sigma}}{\partial \boldsymbol{\varepsilon}} = (1 - D)\boldsymbol{E} - \boldsymbol{E}\boldsymbol{\varepsilon}\frac{\partial D}{\partial \boldsymbol{\varepsilon}} \tag{24}$$

where

$$\frac{\partial D}{\partial \boldsymbol{\varepsilon}} = \frac{\partial D}{\partial \kappa}\frac{\partial \kappa}{\partial \tilde{\varepsilon}}\frac{\partial \tilde{\varepsilon}}{\partial \boldsymbol{\varepsilon}}. \tag{25}$$

With reference to the damage law (17), the first term in (25) is

$$\frac{\partial D}{\partial \kappa} = -\frac{\exp\left(\frac{\kappa - \varepsilon_0}{\varepsilon_0 - \varepsilon_f}\right)\varepsilon_0(\kappa - \varepsilon_0 + \varepsilon_f)}{\kappa^2(\varepsilon_0 - \varepsilon_f)}. \tag{26}$$

The second term can be easily evaluated as

$$\frac{\partial \kappa}{\partial \tilde{\varepsilon}} = \begin{cases} 0 & \text{if } \tilde{\varepsilon} < \kappa \\ 1 & \text{if } \tilde{\varepsilon} = \kappa \end{cases}. \tag{27}$$

Last term is calculated recalling Mazars' definition of the equivalent strain (16). In the plane stress case it results

$$\frac{\partial \tilde{\varepsilon}}{\partial \boldsymbol{\varepsilon}} = \frac{1}{2\tilde{\varepsilon}}(\boldsymbol{P}\langle \boldsymbol{\varepsilon}^p \rangle)^T \tag{28}$$

being

$$\boldsymbol{P} = \begin{bmatrix} 1+\cos(2\alpha) & 1-\cos(2\alpha) & -\frac{2\nu}{1-\nu} \\ 1-\cos(2\alpha) & 1+\cos(2\alpha) & -\frac{2\nu}{1-\nu} \\ \sin(2\alpha) & -\sin(2\alpha) & 0 \end{bmatrix} \tag{29}$$

with α the angle between the principal and the reference directions and ν the Poisson's ratio. $\boldsymbol{\varepsilon}^p$ is the 3 by 1 vector collecting the principal strains. It is remarkable that A-FEM permits different elastic tangent operators for the two sub-elements.

Regarding the interphase element, we adopt the 4-nodes element proposed in [30]. The kinematic and static quantities are referred to the rotated $(x_b,\, z_b)$ reference system. The displacement fields in Σ^+ and Σ^- are expressed as linear interpolation of the displacements of nodes lying in the same Σ^+ and Σ^-:

$$\overline{\mathbf{u}}_b^+ = \mathbf{N}_b^+ \overline{\mathbf{U}}_b^+, \qquad \overline{\mathbf{u}}_b^- = \mathbf{N}_b^- \overline{\mathbf{U}}_b^-, \tag{30}$$

where $\overline{\mathbf{U}}_b^+$ and $\overline{\mathbf{U}}_b^-$ are defined as:

$$\overline{\mathbf{U}}_b^+ = \begin{bmatrix} \overline{\mathbf{U}}_r \\ \overline{\mathbf{U}}_s \end{bmatrix}, \qquad \overline{\mathbf{U}}_b^- = \begin{bmatrix} \overline{\mathbf{U}}_m \\ \overline{\mathbf{U}}_n \end{bmatrix}. \tag{31}$$

The symbol $(\bar{\cdot})$ means that the relative quantity is referred to the interphase coordinate system. Shape functions matrices are expressed as

$$\mathbf{N}_b^+ = \begin{bmatrix} N_2 & 0 & N_1 & 0 \\ 0 & N_2 & 0 & N_1 \end{bmatrix}, \qquad \mathbf{N}_b^- = \begin{bmatrix} N_1 & 0 & N_2 & 0 \\ 0 & N_1 & 0 & N_2 \end{bmatrix}, \tag{32}$$

with

$$N_1 = \frac{1}{2}(1-\xi), \qquad N_2 = \frac{1}{2}(1+\xi), \tag{33}$$

being $\xi \in [-1, 1]$ the natural interphase coordinate.

According to Eq. (2), the interphase strain vector is composed by the contact and internal strains:

$$\boldsymbol{\varepsilon}_b = \frac{1}{w_b}\mathbf{C}_{b_1}\left(\mathbf{u}_b^+ - \mathbf{u}_b^-\right) + \frac{1}{2}\mathbf{C}_{b_2}\left(\mathbf{u}_b^+ + \mathbf{u}_b^-\right) \tag{34}$$

where

$$\boldsymbol{\varepsilon}_b = \begin{bmatrix} \varepsilon_{b_x} & \varepsilon_{b_z} & \gamma_{b_{xz}} \end{bmatrix}^T, \quad \mathbf{C}_{b_1} = \begin{bmatrix} 0 & 0 \\ 0 & 1 \\ 1 & 0 \end{bmatrix}, \quad \mathbf{C}_{b_2} = \begin{bmatrix} \frac{\partial}{\partial x_b} & 0 \\ 0 & 0 \\ 0 & \frac{\partial}{\partial x_b} \end{bmatrix}. \tag{35}$$

Substituting the approximate expression of the displacements (30) we obtain

$$\boldsymbol{\varepsilon}_b = \mathbf{B}_b^+ \overline{\mathbf{U}}_b^+ + \mathbf{B}_b^- \overline{\mathbf{U}}_b^- \tag{36}$$

with

$$\mathbf{B}_b^+ = \left(\frac{1}{w_b} \mathbf{C}_{b_1} + \frac{1}{2} \mathbf{C}_{b_2} \right) \mathbf{N}_b^+, \quad \mathbf{B}_b^- = - \left(\frac{1}{w_b} \mathbf{C}_{b_1} - \frac{1}{2} \mathbf{C}_{b_2} \right) \mathbf{N}_b^-. \tag{37}$$

The weak form of equilibrium for the interphase element can be derived from (4) considering the kinematic equations (30) and (36). Neglecting the external traction applied on the thickness side ($\mathbf{t} = \mathbf{0}$ in Γ_b) we have:

$$\begin{aligned} &\delta \overline{\mathbf{U}}_b^{+T} \int_\Sigma \left(w_b \, \mathbf{B}_b^{+T} \mathbf{E}_t \, \mathbf{B}_b^+ \overline{\mathbf{U}}_b^+ + w_b \, \mathbf{B}_b^{+T} \mathbf{E}_t \, \mathbf{B}_b^- \overline{\mathbf{U}}_b^- - \mathbf{N}_b^{+T} \overline{\mathbf{q}}^+ \right) \mathrm{d}\Gamma + \\ &\delta \overline{\mathbf{U}}_b^{-T} \int_\Sigma \left(w_b \, \mathbf{B}^{b^-{}^T} \mathbf{E}_t \, \mathbf{B}_b^+ \overline{\mathbf{U}}_b^+ + w_b \, \mathbf{B}_b^{-T} \mathbf{E}_t \, \mathbf{B}_b^- \overline{\mathbf{U}}_b^- - \mathbf{N}_b^{-T} \overline{\mathbf{q}}^- \right) \mathrm{d}\Gamma = 0 \end{aligned} \tag{38}$$

which, being satisfied for any value of virtual displacements, gives

$$\overline{\mathbf{K}}_b^{++} \overline{\mathbf{U}}_b^+ + \overline{\mathbf{K}}_b^{+-} \overline{\mathbf{U}}_b^- = \overline{\mathbf{F}}_b^+ \tag{39}$$

$$\overline{\mathbf{K}}_b^{-+} \overline{\mathbf{U}}_b^+ + \overline{\mathbf{K}}_b^{--} \overline{\mathbf{U}}_b^- = \overline{\mathbf{F}}_b^- \tag{40}$$

where

$$\overline{\mathbf{K}}_b^{++} = \int_\Sigma w_b \, \mathbf{B}_b^{+T} \mathbf{E}_t \, \mathbf{B}_b^+ \mathrm{d}\Gamma, \qquad \overline{\mathbf{K}}_b^{+-} = \int_\Sigma w_b \, \mathbf{B}_b^{+T} \mathbf{E}_t \, \mathbf{B}_b^- \mathrm{d}\Gamma, \tag{41}$$

$$\overline{\mathbf{K}}_b^{-+} = \int_\Sigma w_b \, \mathbf{B}_b^{-T} \mathbf{E}_t \, \mathbf{B}_b^+ \mathrm{d}\Gamma, \qquad \overline{\mathbf{K}}_b^{--} = \int_\Sigma w_b \, \mathbf{B}_b^{-T} \mathbf{E}_t \, \mathbf{B}_b^- \mathrm{d}\Gamma. \tag{42}$$

Note that the same expression (24) of the elastic tangent operator for bulk material is adopted.

3.2. Assembling procedure

In order to assembly the three finite elements we have to refer the kinematic and static quantities to the global reference system. Since the orientation of the band is individuated by the unit vector $\mathbf{n}_b = \begin{bmatrix} n_x & n_z \end{bmatrix}^T$, we can proceed with a reference system rotation in a classical way:

$$\overline{\mathbf{U}}_b^{(-,+)} = \mathbf{R}\mathbf{U}_b^{(-,+)} \qquad \mathbf{F}_b^{(-,+)} = \mathbf{R}^T\overline{\mathbf{F}}_b^{(-,+)} \tag{43}$$

where

$$\mathbf{R} = \begin{bmatrix} n_z & -n_x & 0 & 0 \\ n_x & n_z & 0 & 0 \\ 0 & 0 & n_z & -n_x \\ 0 & 0 & n_x & n_z \end{bmatrix}. \tag{44}$$

The substitution of Eqs. (43) in Eqs. (41) provides the equilibrium equations of the interphase element written in the global reference system.
Partitioning the displacement vectors $\mathbf{U}^+$ and $\mathbf{U}^-$ of the sub-elements into external (e) and internal (i) components, in relation to the Ω_b domain, the following partitioned Eq (20) is derived:

$$\begin{bmatrix} \mathbf{F}_{ee}^{(-,+)} \\ \mathbf{F}_{ei}^{(-,+)} \end{bmatrix} + \begin{bmatrix} \mathbf{0} \\ \mathbf{F}_{ii}^{(-,+)} \end{bmatrix} = \begin{bmatrix} \mathbf{K}_{ee}^{(-,+)} & \mathbf{K}_{ei}^{(-,+)} \\ \mathbf{K}_{ie}^{(-,+)} & \mathbf{K}_{ii}^{(-,+)} \end{bmatrix} \begin{bmatrix} \mathbf{U}_e^{(-,+)} \\ \mathbf{U}_i^{(-,+)} \end{bmatrix}. \tag{45}$$

It is easy to verify that:

$$\mathbf{U}_b^+ = \mathbf{A}\mathbf{U}_i^+, \quad \mathbf{U}_b^- = \mathbf{A}\mathbf{U}_i^-, \tag{46}$$

being $\mathbf{A}$ an operator defined as

$$\mathbf{A} = \begin{bmatrix} \mathbf{0} & \mathbf{I} \\ \mathbf{I} & \mathbf{0} \end{bmatrix}, \tag{47}$$

with $\mathbf{0}$ and $\mathbf{I}$ 2×2 null and identity blocks, respectively.
Substituting Eqs. (46) in the interphase equilibrium equations (39)-(40) and pre-multiplying the right and left sides of the same equations by the order operator $\mathbf{A}$, finally we have

$$\mathbf{K}_b^{++}\mathbf{U}_i^+ + \mathbf{K}_b^{+-}\mathbf{U}_i^- = \mathbf{F}_{ii}^+, \tag{48}$$
$$\mathbf{K}_b^{-+}\mathbf{U}_i^+ + \mathbf{K}_b^{--}\mathbf{U}_i^- = \mathbf{F}_{ii}^-, \tag{49}$$

where

$$\mathbf{K}_b^{\iota\kappa} = \mathbf{L}^T \overline{\mathbf{K}}_b^{\iota\kappa} \mathbf{L}, \quad \mathbf{F}_{ii}^{\iota} = \mathbf{L}^T \bar{\mathbf{F}}_b^{\iota} \quad \text{with} \quad \iota, \kappa \in \{+, -\} \tag{50}$$

and $\mathbf{L} = \mathbf{R}\mathbf{A}$.

We can substitute the expression of the internal forces (48)-(49) in the equilibrium equations of the sub-elements (45) in order to evaluate the internal displacements:

$$\mathbf{U}_i^+ = \mathbf{H}^+ \left[\mathbf{F}_{ei}^+ - \mathbf{K}_{ie}^+ \mathbf{U}_e^+ + \mathbf{M}^+ \left(\mathbf{F}_{ei}^- - \mathbf{K}_{ie}^- \mathbf{U}_e^- \right) \right], \tag{51}$$

$$\mathbf{U}_i^- = \mathbf{H}^- \left[\mathbf{F}_{ei}^- - \mathbf{K}_{ie}^- \mathbf{U}_e^- + \mathbf{M}^- \left(\mathbf{F}_{ei}^+ - \mathbf{K}_{ie}^+ \mathbf{U}_e^+ \right) \right], \tag{52}$$

with

$$\mathbf{H}^+ = \left[\mathbf{K}_{ii}^+ - \mathbf{K}_b^{++} - \mathbf{K}_b^{+-} \left(\mathbf{K}_{ii}^- - \mathbf{K}_b^{--} \right)^{-1} \mathbf{K}_b^{-+} \right]^{-1} \tag{53}$$

$$\mathbf{H}^- = \left[\mathbf{K}_{ii}^- - \mathbf{K}_b^{--} - \mathbf{K}_b^{-+} \left(\mathbf{K}_{ii}^+ - \mathbf{K}_b^{++} \right)^{-1} \mathbf{K}_b^{+-} \right]^{-1} \tag{54}$$

$$\mathbf{M}^+ = \mathbf{K}_b^{+-} \left(\mathbf{K}_{ii}^- - \mathbf{K}_b^{--} \right)^{-1} \tag{55}$$

$$\mathbf{M}^- = \mathbf{K}_b^{-+} \left(\mathbf{K}_{ii}^+ - \mathbf{K}_b^{++} \right)^{-1}. \tag{56}$$

Finally, the equilibrium equations of the single quadrilateral element with embedded interphase are obtained:

$$\begin{bmatrix} \mathbf{F}_{ee}^- - \mathbf{K}_{ei}^- \mathbf{H}^- \left(\mathbf{F}_{ei}^- + \mathbf{M}^- \mathbf{F}_{ei}^+ \right) \\ \mathbf{F}_{ee}^+ - \mathbf{K}_{ei}^+ \mathbf{H}^+ \left(\mathbf{F}_{ei}^+ + \mathbf{M}^+ \mathbf{F}_{ei}^- \right) \end{bmatrix} = \begin{bmatrix} \mathbf{K}_{ee}^- - \mathbf{K}_{ei}^- \mathbf{H}^- \mathbf{K}_{ie}^- & -\mathbf{K}_{ei}^- \mathbf{H}^- \mathbf{M}^- \mathbf{K}_{ie}^+ \\ -\mathbf{K}_{ei}^+ \mathbf{H}^+ \mathbf{M}^+ \mathbf{K}_{ie}^- & \mathbf{K}_{ee}^+ - \mathbf{K}_{ei}^+ \mathbf{H}^+ \mathbf{K}_{ie}^+ \end{bmatrix} \begin{bmatrix} \mathbf{U}_e^- \\ \mathbf{U}_e^+ \end{bmatrix}. \tag{57}$$

The above-presented formulation of the finite element with the embedded localization zone has the peculiar feature that the two sub-elements and the interphase in which the initial element is split share the same constitutive model. Other than band thickness, no additional material parameters and evolution laws are needed. As compared to similar approaches using the zero-thickness interface for localization and fracture simulation, this represents an important advantage. In the ZTI model, an additional cohesive law must be introduced, with the difficulty of evaluating the additional material parameters in some way related to those of the continuum model.

4. Numerical procedure at the structural model level

In the present section the macroscale (or structural-scale) problem is focused. It requires the formulation of an algorithm capable of predicting the formation and propagation of the band/fracture among the finite elements of the numerical model.
This issue has been treated in several papers, with the principal aim to make the fracture pattern independent of the finite elements density and orientation.
When the strain localization band is not known a priori, the principal issues include:

- the strain localization band formation;
- location and orientation of the localization band;
- the intra-element propagation of the fracture;
- identification of the crack pattern and the coexistence of multiple cracks.

The first two aspects are strongly related to the constitutive model adopted for the quasi-brittle material. The remaining ones deal with finite element mesh processing. They require a specific crack tracking algorithm in order to define the discontinuity surface during the loading process. In addition, they require the introduction of additional degrees of freedom to describe the kinematics of the weak or strong discontinuity.
The entire numerical procedure has been implemented in a MatLab© code. Nonlinear equations are solved using the Newton-Raphson iterative procedure. The time integration scheme is based on a backward Euler method. For the sake of completeness, the pseudo-code for the generic time step n is reported in Algorithm 1.

4.1. Band formation and orientation

As mentioned in the introduction, the onset of localized deformations is considered as the result of an instability in the macroscopic constitutive description of inelastic deformation. It corresponds to a bifurcation problem [1, 2], i.e. the incremental equations governing the equilibrium show a loss of uniqueness and an alternative deformation mode of the evolution of the localization band is admitted. Commonly, the discontinuous bifurcation condition is determined by the negative value of the determinant of the acoustic

tensor [34]. A spectral analysis of the same tensor also provides band orientation and relative localization mode.
In the case of isotropic damage, where the material stiffness degradation simply coincides with the progressive reduction of the Young's modulus, the above reported classical procedure under some circumstances does not return the expected band characteristics. In particular, band directions that don't match the loading conditions and kinematic constraints may be observed [35]. In several works adopting the continuous-discontinuous models a specific transition criterion is formulated in terms of principal stresses, principal strains, or damage values locally attained. If the state of stress or strain is considered as a strain localization indicator, the Rankine or the De Saint Venant - Grashof criteria are adopted, respectively. When the maximum principal stress or strain reaches the tensile strength or the limit deformation of the material, the condition of diffuse damage is switched to the condition of localized damage.
In the present work the continuous-discontinuous transition is triggered if simultaneously the minimum eigenvalue of the element tangent stiffness matrix becomes null or negative and if the damage variable attains a critical value D_{crit}, as proposed in [36]. This last criterion has been adopted in recent papers dealing with localization in structures made up of damaging material [37, 38].
In particular, if the volume average of the damage variable exceeds the critical damage of the material a new interphase is inserted in the element. The transition condition reads

$$\hat{D} = \frac{1}{V_e} \int_{\Omega_e} D \, \mathrm{d}\Omega \; > \; D_{crit}, \tag{58}$$

where V_e is the volume of the element.
In order to locate the interphase middle plane inside the finite element, we define the balance point of damage $\mathbf{x}_{bp}$

$$\mathbf{x}_{bp} = \frac{\sum_{i=1}^{ngp} D_i \, \mathbf{x}_i}{\sum_{i=1}^{ngp} D_i} \tag{59}$$

and the average localization direction $\mathbf{n}_b$, which coincides with the eigenvector associated with the maximum eigenvalue of the following tensor:

$$\mathbf{L}_b = \frac{\sum_{i=1}^{ngp} D_i \, \mathbf{n}_i \otimes \mathbf{n}_i}{\sum_{i=1}^{ngp} D_i}, \tag{60}$$

where ngp is the number of the Gauss points and $\mathbf{x}_i$ and D_i are the coordinates and the values of damage variable at the same points, respectively. In Eq. (60) $\mathbf{n}_i$ is the direction of the maximum principal strain evaluated at the Gauss point.

Once the first two localization conditions are verified, a third check is performed. This check verifies if the localization direction $\mathbf{n}_b$ is stabilized between two subsequent time steps [39]. When the difference in $\mathbf{n}_b$ is below a fixed tolerance, the finite element is fragmented into two sub-elements Ω^+ and Ω^-, and the interposed interphase Ω_b. Depending on the topology of the two sub-elements, strain and damage values can be initialized at Gauss points of Ω^+, Ω^-, and Ω_b, exploiting the same shape functions as the original element. Damage in the sub-elements Ω^+ and Ω^- is kept frozen and the response is linear and elastic, with the stiffness attained at the fragmentation time. Damage, instead, is free to evolve in the interphase element Ω_b.

4.2. Crack tracking algorithm

At the end of the strain localization stage in Algorithm 1, some of the elements of the FE mesh could be localized. For these elements the three aforementioned localization checks are all verified and the band in each element is identified through its balance point and orientation.

The number of newly localized elements in a load step is dependent on the load step size. As is common in nonlinear FE, in order to avoid inaccurate solutions in terms of crack-path and mechanical response, the load step should be in some way calibrated to the element size and should not be too large. It could happen to see clouds of localized elements, usually having sub-parallel localization bands, as a consequence of the diffuse damage formulation. In these cases not all the localized elements can be crossed by the crack and the clouds need to be in a certain sense 'cleaned'.

An efficient crack tracking algorithm is therefore necessary to correctly transform the bands inside localized elements into macroscopic continuous cracks. The proposed crack tracking algorithm operates in a three-stage process.

Algorithm 1 Pseudo-Code at step n

▷ Update BCs and/or ext. forces

► **ELASTIC PREDICTION**

$j \leftarrow 1$ ▷ Initialize iterations

$\mathbf{U}_n \leftarrow \mathbf{U}_{n-1}$ ▷ Initialize $\mathbf{U}_n$

$\mathbf{F}_n^{ext} \leftarrow \mathbf{F}_{n-1}^{ext} + \Delta\mathbf{F}_n^{ext}$ ▷ Update ext. forces

$\mathbf{K}_n^{(j)} \leftarrow \mathrm{A}_{e=1}^{e_{no-loc}}(\mathbf{K}_{n-1}^e) + \mathrm{A}_{s=1}^{subs}(\mathbf{K}_{n-1}^s)$ ▷ Assemble global stiffness matrix

$\mathbf{K}_n^{(j)}\,\Delta\mathbf{U}_n^{(j)} = \Delta\mathbf{F}_n^{ext}$ ▷ Solve equilibrium equations

$\mathbf{U}_n \leftarrow \mathbf{U}_n + \Delta\mathbf{U}_n^{(j)}$ ▷ Update mech. & kin. variables

for $s = 1 : subs$ **do** ▷ Loop over all substructures

  $\mathbf{U}_n^s \leftarrow S(\mathbf{U}_n)$ ▷ Extract displ. at subs boundary nodes

  $\mathbf{F}_n^{int,\,s} \leftarrow$ CALL SOLVE-SUBS($\mathbf{U}_n^s$) ▷ Solve NL problem for subs imposing $\mathbf{U}_n^s$

end for

$\mathbf{F}_n^{int} \leftarrow \mathrm{A}_{e=1}^{e_{no-loc}}(\mathbf{F}_n^{int,e}) + \mathrm{A}_{s=1}^{subs}(\mathbf{F}_n^{int,s})$ ▷ Assemble int force vector

if $\left|\mathbf{Err}_n^{(j)}\right| = \left|\mathbf{F}_n^{ext} - \mathbf{F}_n^{int}\right| \geq tol$ **then** ▷ check convergence

► **NONLINEAR CORRECTION**

  $j \leftarrow j + 1$

  $\mathbf{K}_n^{(j)} \leftarrow \mathrm{A}_{e=1}^{e_{no-loc}}(\mathbf{K}_n^e) + \mathrm{A}_{s=1}^{subs}(\mathbf{K}_n^s)$ ▷ Assemble global stiffness matrix

  $\mathbf{K}_n^{(j)}\,\Delta\mathbf{U}_n^{(j)} = \mathbf{Err}_n^{(j)}$ ▷ Solve equilibrium equations

  go to 7

end if

► **STRAIN LOCALIZATION**

for $e = 1 : e_{no-loc}$ **do** ▷ Loop over not localized elements

  $\lambda^e \leftarrow eig[\mathbf{K}^e]$ ▷ Find tangent stiffness eigenvalues

  $\hat{D}^e \leftarrow \frac{1}{V_e}\int_{\Omega_e} D\,\mathrm{d}\Omega$ ▷ Calculate volume average of damage

  if $(\lambda^e \leq 0)\,.and.\,(\hat{D}^e \geq D_{crit})$ **then** ▷ Check localization

    $\mathbf{x}_{bp}, \mathbf{L}_b \leftarrow$ Use Eqs.(59-60) ▷ Find balance point & loc. tensor

    $\mathbf{n}_b \leftarrow eig[\mathbf{L}_b]$ ▷ Evaluate band orientation

    if $\left|\mathbf{n}_b^n - \mathbf{n}_b^{n-1}\right| \leq tol$ **then** ▷ Check band stabilization

      $\mathbf{e}_{loc} \leftarrow [\mathbf{e}_{loc}\ e]$ ▷ Insert e among new localized elements

    end if

  end if

end for

► **CRACK TRACKING ALGORITHM**

clusters $\leftarrow$ CALL NO-BINARY-SEARCH($\mathbf{e}_{loc}$) ▷ Partition of $\mathbf{e}_{loc}$ into clusters

subs $\leftarrow$ CALL UPDATE-SUBS(clusters) ▷ Update existing subs or create new ones

CALL ALIGN(subs) ▷ Align bands in new localized elements

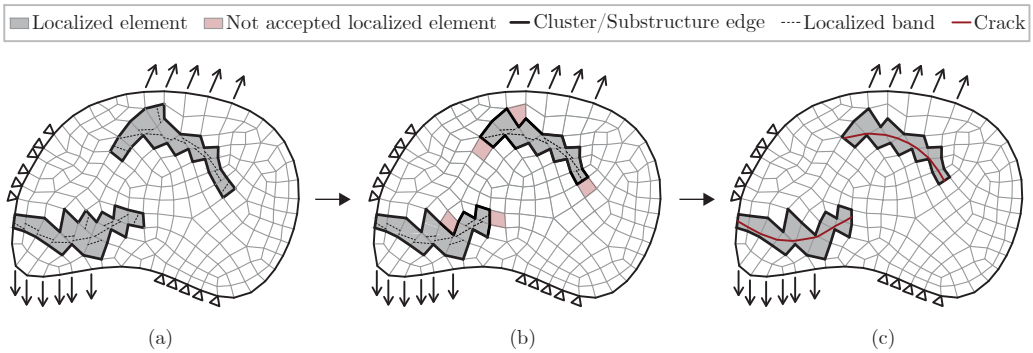

Figure 5: Three-stage process of the crack tracking algorithm. a) Clusters identification. b) Substructures identification. c) Alignment of bands in substructures.

This process is depicted in a simplified manner in Figure 5. The first stage groups the newly localized elements into clusters of elements that are at least two-by-two in contact (Fig. 5a). The associated numerical procedure is inspired by the No Binary Search contact detection algorithm [40].
The second stage transforms each cluster into a substructure (Fig. 5b). At this stage, only the localized elements required to maintain a continuous crack are retained, converting the remaining elements back into not localized elements again. The selection is carried out on the basis of specific checks that will be introduced in the next sub-paragraph.
The third stage deals with crack propagation among elements and performs the alignment of bands in order to have continuous cracks (Fig. 5c).
The crack tracking algorithm has been numerically structured into three correspondent in-series modules, namely the `NO-BINARY-SEARCH MODULE` (Algorithm 1, line 30), the `UPDATE-SUBS MODULE` (Algorithm 1,line 31), and the `ALIGN MODULE` (Algorithm 1, line 32).

4.2.1. Substructures of localized elements

In the second stage of the crack tracking algorithm clusters are converted into substructures. These substructures can be defined as portions of the whole model containing those elements intersected by a single crack. It follows that under specific circumstances not all the elements of a cluster can be part of a substructure and they need to be opportunely shortlisted.
Selection is made on the basis of a total of four checks. Some of these are consolidated in the literature, while others are specifically designed according to the adopted localization criteria. Two of these checks are always invoked,

and two are recalled if the new localized elements extend an existing crack. All the four checks are clearly explained in Fig. 6 and listed below:

- the scalar product between the vector $\mathbf{v}$ linking the crack tip and the centroid of the new localized element and the outgoing versor $\mathbf{n}$ normal to the edge of the element containing the crack tip must be positive, in order to avoid coming back fractures (Fig. 6a):

$$\mathbf{v} \cdot \mathbf{n} > \mathbf{0};$$

- band orientations in two adjacent localized elements must not differ more than a prescribed limit (Fig. 6b);

- in the presence of parallel bands in adjacent elements only one crack is generated. The accepted elements to be part of a substructure are those whose band extremes share the same edge (Fig. 6c). In the case of a crack involving a single element, the element showing the highest value of the damage variable $\hat{D}$ is retained (Fig. 6d).

No 'a priori' initialization of a crack is required, and multiple cracks are admitted.

4.2.2. Crack propagation

The last part of the crack tracking algorithm is devoted to the alignment of bands in elements constituting the substructure, in order to guarantee crack-path continuity. Three possibilities arise:

1. extension of existing cracks;
2. merging of existing cracks;
3. formation of a new crack.

In general, new elements are usually added to an existing crack. In this circumstance, the constraint that the band should pass through the balance point is relaxed, while the localization direction is maintained (Fig. 7a). The balance point is replaced by the previous crack tip position, and the band results shifted inside the element. If more than one element is added, the procedure continues with the next element on the list, until the entire list is completed. In order to ensure continuity of deformation between the element containing the new crack tip and the adjacent not localized element sharing the same edge, the new internal nodes placed on the crack tip must move

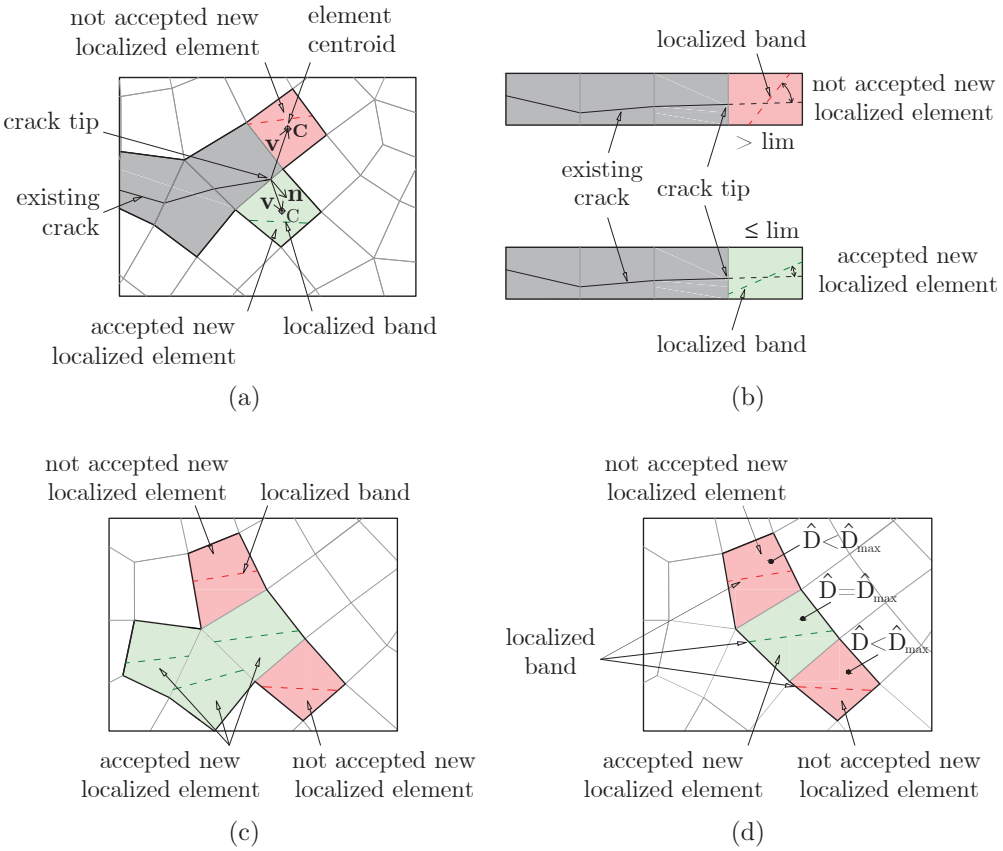

Figure 6: Substructures of localized elements. a) element centroid position check; b) band slope check; c) new crack length check; d) $\hat{D}$ check.

together and lie on the same edge. This constraint is removed once a new element is added to the substructure and the crack tip moves ahead.

If the new substructure comes from the fusion of two substructures, old cracks are initially extended following the same procedure as in point 1. Occasionally, two existing cracks should be extended with the same element, which is referred to as an enclosed element (Fig. 7b). The previous crack tips are directly connected in this case. Additionally, nodes constrained to coincide with the two old crack tips are released.

Once the existing cracks have been scanned over, the remaining new cracks are inserted starting from the middle element towards the extremes. For the first element the band is inserted as localized, since both the balance

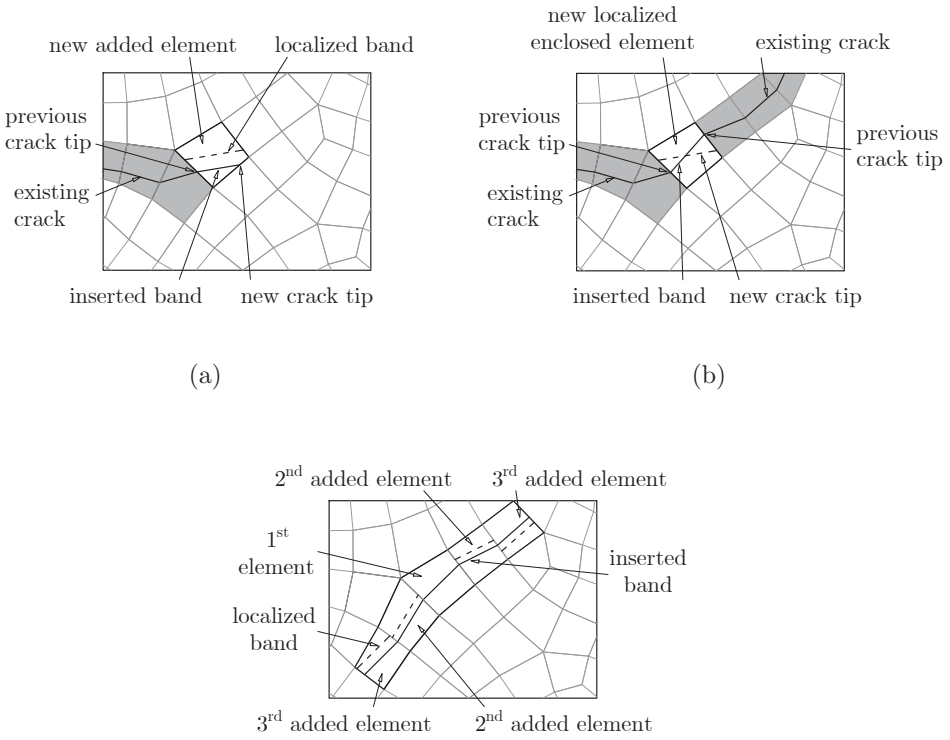

Figure 7: Crack propagation. a) addition of a new element; b) addition of an enclosed element; c) insertion of a new crack with more than one element.

point and localization band orientation are maintained. For the subsequent elements the balance point is substituted by the crack tip, while the band orientation remains unchanged as for the previous point 1 (Fig. 7c).

The key point of the numerical procedure is to split at the generic time step the solution of the substructures from the solution of the remaining part of the finite element model. In this sense the procedure contemplates two nested nonlinear iterative procedures. One procedure is at the substructure level, where the nodal displacements act as boundary essential conditions, and the other is at the model level. At the substructure level, the Newton-Raphson iterative procedure leads to the correspondent boundary nodal forces together

Table 1: Example 1 - Material parameters

$E\ [MPa]$	ν	ε_0	$\frac{\varepsilon_f}{\varepsilon_0}$	$w_b\ [mm]$	D_{crit}
1000	0.2	$1.0E-3$	100	1	0.1

with the updated substructure stiffness matrix. The stiffness matrix and the nodal forces contribute to in turn updating the stiffness matrix and internal force vector of the whole structure.

5. Numerical applications

In order to show the effectiveness of the proposed numerical method, in this section the results of four applications ranging from mode I and combined mode I-mode II loading stress states are reported. Each application is performed under plane stress and under displacement control.
In Example 1 a single edge notched specimen is loaded in order to create a mixed mode I-mode II stress state. This example shows the capability of the crack tracking algorithm to follow the correct crack pattern in the absence of mesh dependency. The same example is also run with three different load step sizes in order to analyze the influence of load step size on the results and on the convergence of the iterative solution.
A classical three-point bending test is examined in Example 2. In order to strengthen mesh independence and investigate the interphase thickness parameter, two simple meshes are used to discretize the fracture propagating zone.
In Example 3 a mode I test on a double edge notched specimen is run. The peculiarity of this example resides in the double crack propagation and the comparison of the overall response with the analogous test run by Benvenuti et al. [41] who used the regularized X-FEM method.
Finally, Example 4 illustrates the ability of the code to reproduce the experimental results for a double edge notched specimen under a combination of mode I - mode II stress states. The same example is exploited to show a comparison between the IPH model and the ZTI model.

5.1. Example 1: single edge notched specimen under mixed mode

A $100 \times 100\ mm$ specimen with a unitary thickness and a non-symmetric notch is analyzed (Fig. 8). Adopted material parameters are reported in

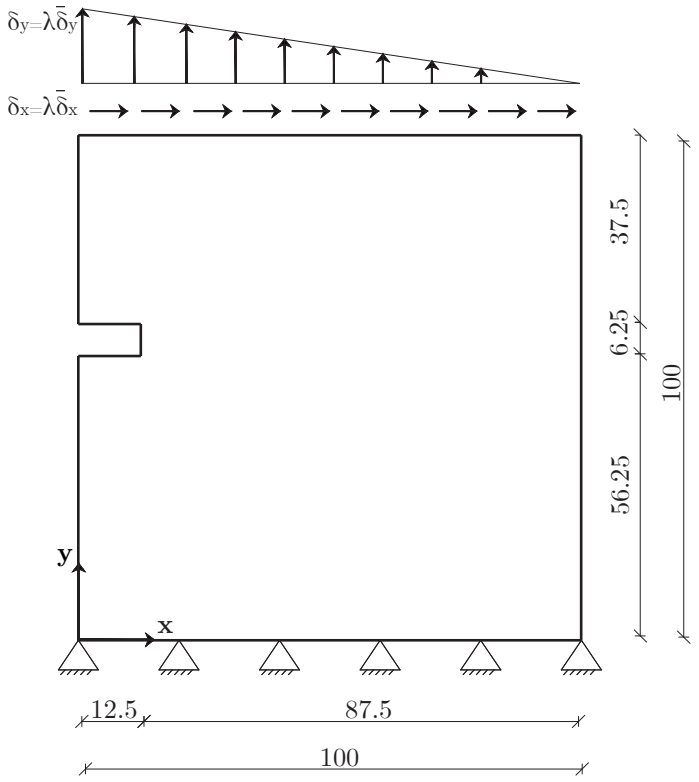

Figure 8: Example 1 - Geometry and boundary conditions. Measures are expressed in mm.

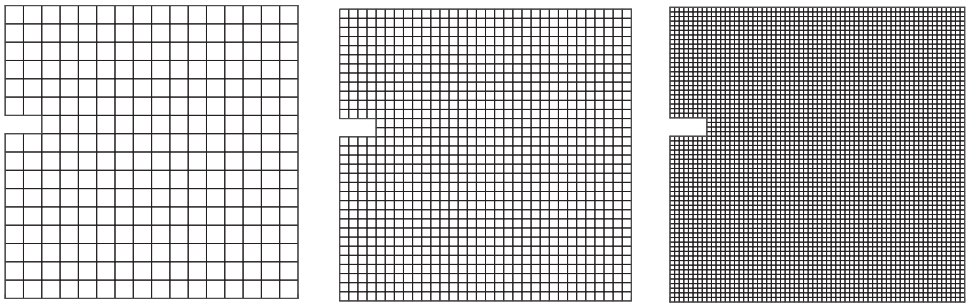

Figure 9: Example 1. Different employed RM: a) 16×16, b) 32×32, c) 64×64.

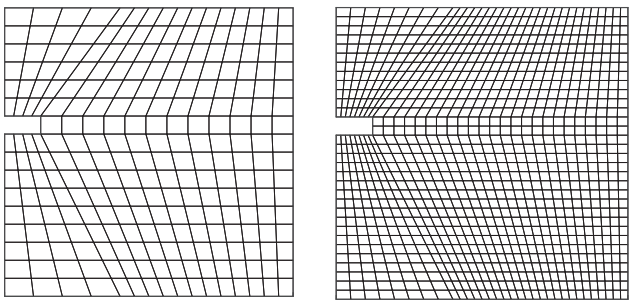

(a) (b)

Figure 10: Example 1. Different employed SM: a) 16×16, b) 32×32.

Table 1. The specimen is constrained on the bottom side and the upper edge is subjected to uniform horizontal displacements together with linear vertical displacements. These displacements are maximum on the left node and zero on the right node.

The final values of horizontal and maximum vertical displacements are fixed to $\bar{\delta}_x = 0.85\ mm$ and $\bar{\delta}_y = 1\ mm$ respectively. In order to investigate mesh size and orientation, the example is run using five different meshes, consisting of three regular meshes (RM) and two skewed meshes (SM). The three RM are reported in Figure 9a-c where, respecting a classical h-refinement rule, the three meshes are composed of 16×16, 32×32, and 64×64 quadrilateral linear elements. The two SM are instead depicted in Figure 10 using 16×16 (Fig. 10a) or 32×32 (Fig. 10b) quadrilateral linear elements respectively.

Each crack originates in the notch and propagates in the direction of the right edge of the specimen, maintaining the same inclination throughout. Final fracture patterns are reported in Figure 11b. Cracks are nearly overlapped, with a slight difference due to mesh size. No influence is observed due to mesh orientation. This is a remarkable result, since it is known from the literature [42] how much the application of a bias factor to the mesh influences the response. Load-displacement curves are in good agreement between each other, confirming the almost absence of mesh-dependence of the response (see Fig. 11a).

The implemented constitutive model returns nonlinear behavior with softening. After the initial elastic phase, the highest principal strains nearby the notch lead to strain localization and crack propagation. The nonlinear phase reaches its peak at around 45 N, beyond which cracks develop faster dividing

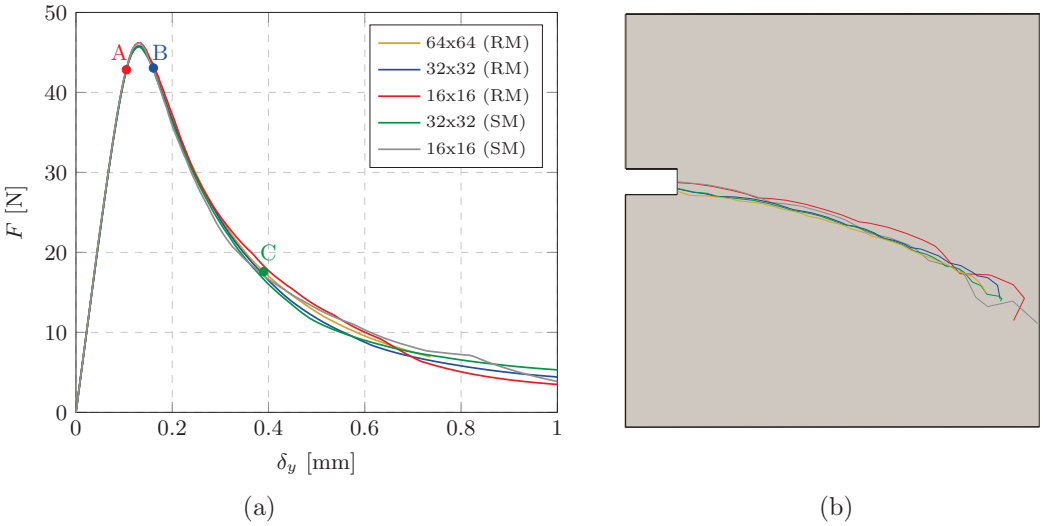

Figure 11: Example 1 - (a) Load-displacement curves; (b) Crack patterns. Markers A, B, C indicate three states for which the deformed shapes are plotted in Figure (12).

the specimen into an upper and a lower block.

In Figure 12 the deformed shape and crack pattern for the 64×64 RM are reported at the three marked points of Figure 11a, corresponding to a $\bar{\delta}_y$ multiplier λ equal to 0.105 (point A), 0.161 (point B), 0.390 (point C) respectively. The crack extends from the lower part of the notch to the opposite edge of the specimen in a curved path. At point C crack mouth opening displacement reaches a value of 0.42 mm.

The same test is run on the 32×32 SM in order to show the convergence behavior of the numerical code. Three different load step sizes are considered, so that the influence of load step size can be highlighted. In the first test the amplitude of the imposed vertical displacement in the step is equal to $\Delta\delta_y = 2 \cdot 10^{-4}$ mm, for a total of 5000 steps. In the second and third tests the step size is 10 times and 15 times larger than the first test, respectively. The results in terms of load-displacement curves are shown in Figure (13a). As expected from the literature, a loading increment influences the peak force value for a fixed grid spacing. Additionally, the crack patterns exhibit differences in their final parts (Fig. 13b), resulting in different residual loads. The difference in the residual loads could be explained considering the different amount of elements remaining between the crack and the right edge

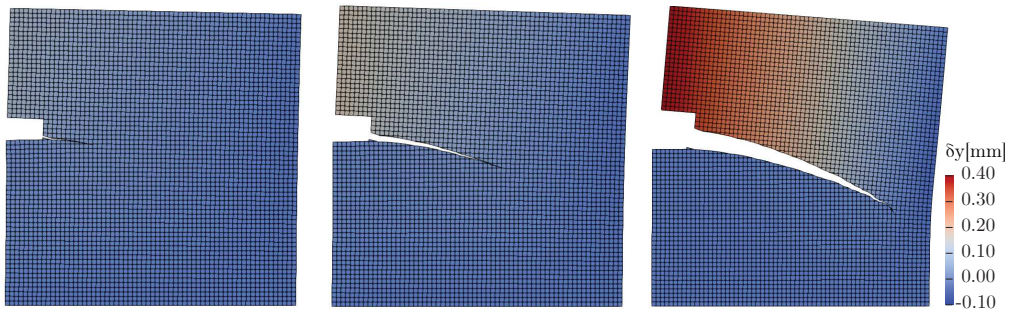

Figure 12: Example 1 - Deformed shape at points (a) A, (b) B, and (c) C indicated in Figure (11)a.

of the specimen. This constitutes a sort of rotational hinge with a different stiffness.

Convergence data are reported in Tables (2)-(3) and (4) for the same multipliers λ (A, B, C) and for each load step size respectively. In each table the errors at the end of the global time steps are reported, together with the number of iterations used to reach convergence at the substructure level. As the load step size is increased, quadratic convergence is assured and the number of iterations increases.

Table 2: Example 1 - Convergence data with $\Delta\delta_y = 2 \cdot 10^{-4}\ mm$.

Glob. n_{it}	A (Step 525) Error	A (Step 525) Total n. loc. iter.	B (Step 805) Error	B (Step 805) Total n. loc. iter.	C (Step 1950) Error	C (Step 1950) Total n. loc. iter.
1	1.11E-4	3	5.48E-5	3	3.61E-6	2
2	5.13E-10	3	3.49E-10	3	2.53E-13	2
3	1.05E-14	3	2.92E-14	3	-	-

5.2. Example 2: three-point bending test

In this example, the embedded interphase model is tested on a classical three-point bending test, for which it is known that crack formation occurs in pure mode I.

The specimen has unitary thickness. Geometry and boundary conditions are

Table 3: Example 1 - Convergence data with $10\Delta\delta_y$.

Glob. n_{it}	A (Step 52)		B (Step 80)		C (Step 195)	
	Error	Total n. loc. iter.	Error	Total n. loc. iter.	Error	Total n. loc. iter.
1	2.22E-2	4	8.12E-3	3	1.60E-3	3
2	2.05E-3	4	4.35E-6	3	1.36E-7	3
3	1.85E-8	4	9.76E-13	3	1.12E-13	3
4	9.12E-15	4	-	-	-	-

Table 4: Example 1 - Convergence data with $15\Delta\delta_y$.

Glob. n_{it}	A (Step 34)		B (Step 54)		C (Step 130)	
	Error	Total n. loc. iter.	Error	Total n. loc. iter.	Error	Total n. loc. iter.
1	3.11E-1	5	3.30E-1	4	9.89E-4	3
2	3.83E-2	4	1.38E-2	4	2.22E-8	3
3	1.59E-4	4	2.49E-3	4	1.15E-13	3
4	6.05E-9	4	4.20E-8	4	-	-
5	1.01E-14	4	1.91E-14	4	-	-

reported in Figure 14. Material parameters are given in Table 5.
Due to the simple crack evolution in this case (only vertical fracture), the real purpose of the test is to examine the effect of interphase thickness. Moreover, this example gives us the chance to highlight the advantages of this model with respect to the classic diffused crack model. In fact, it is known that a diffused crack model suffers mesh dependency since damage is spread over the element. For example, let us consider the two different meshes adopted for the strip above the notch, as shown in Figure 15. In particular, the mesh in Figure 15a (M1) has one vertical row of elements, with the same width as the notch width (5 mm). In contrast, the mesh in Figure 15b (M2) has three vertical rows of elements, each with a width equal to one third of the notch width (5/3 mm). The mesh outside the localization zone is left unchanged. All the elements are quadrilateral and linear.

Initially two tests are run employing the diffused approach with the two M1 and M2 meshes, till a final displacement $\bar{\delta}_y = 0.5\ mm$. The resulting nonlinear behavior is represented by the load-displacement curves plotted as

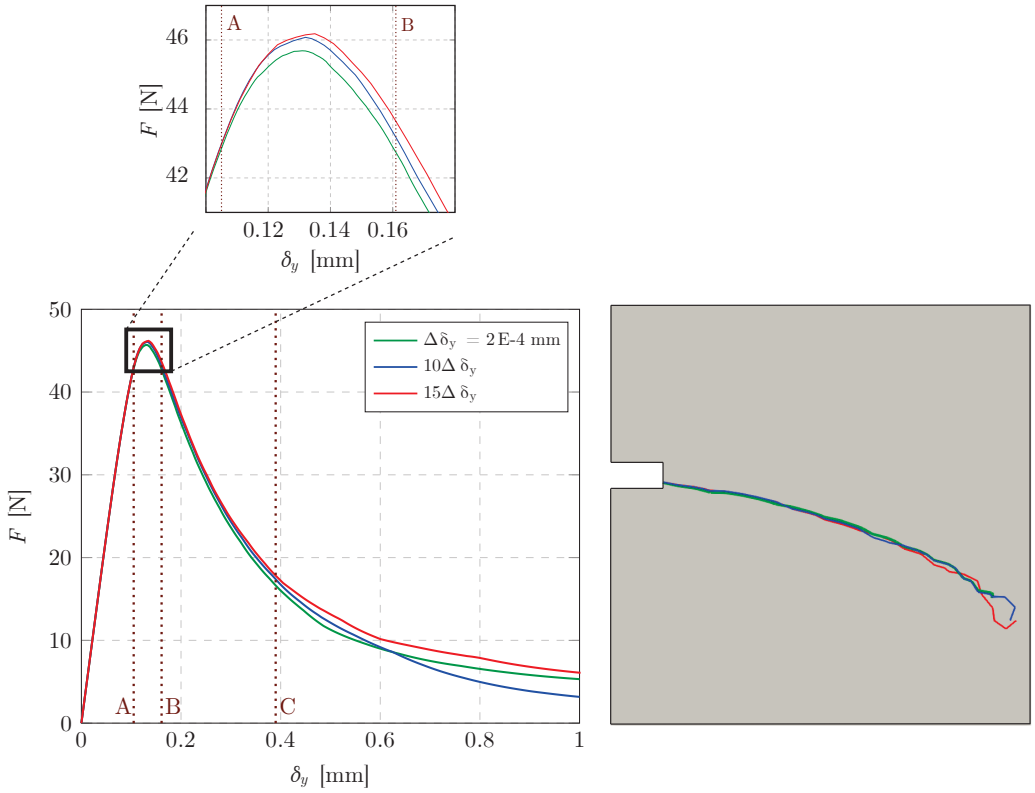

Figure 13: Example 1 - Influence of the load step size: a) Load-displacement curves; b) crack patterns.

dotted lines in Figure 16. Since damage localizes in elements of different widths and is more concentrated when thinner elements are adopted, a lower load-displacement curve is obtained when the M2 mesh is used. Considering that the same material parameters are used for both meshes, the different results are due to mesh size.

Now, the same test is run on M1 mesh using the proposed model, varying the interphase thickness from 0.5 mm to 5 mm. As it is shown in Figure 16, a wider thickness leads to a higher load-displacement curve, as expected. Moreover, when the interphase thickness equals the element width of M1 or M2 mesh, the load-displacement curve overlaps the corresponding dotted

Table 5: Example 2 - Material parameters

$E\ [MPa]$	ν	ε_0	$\frac{\varepsilon_f}{\varepsilon_0}$	D_{crit}
20000	0.2	$1.2E-4$	58	0.5

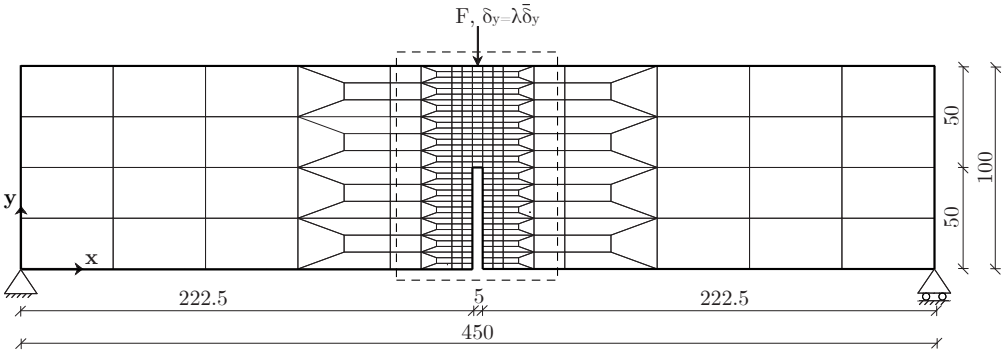

Figure 14: Example 2 - Geometry and boundary conditions. Measures are expressed in mm.

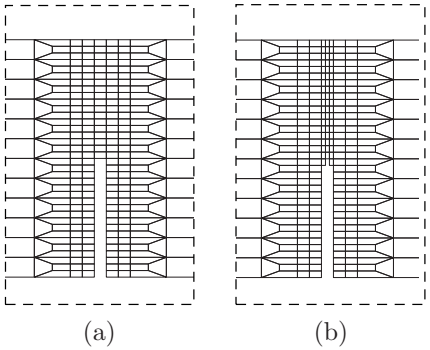

Figure 15: Example 2 - a) Mesh 1 (M1); b) Mesh 2 (M2).

line, making the outcome independent of mesh.
In Figure 17 a comparison between diffused (on the left) and proposed approach (on the right) is reported in terms of damage distribution and deformed shape at a multiplier $\lambda = 0.24$ of the final imposed displacement. Figure 17a refers to points A of Figure 16, while Figure 17b to points B. Since the proposed model freezes damage outside the interphase (not visible in Figure 17) after element localization, the damage maps look less intense with respect to the diffused approach, where damage is distributed over the elements.

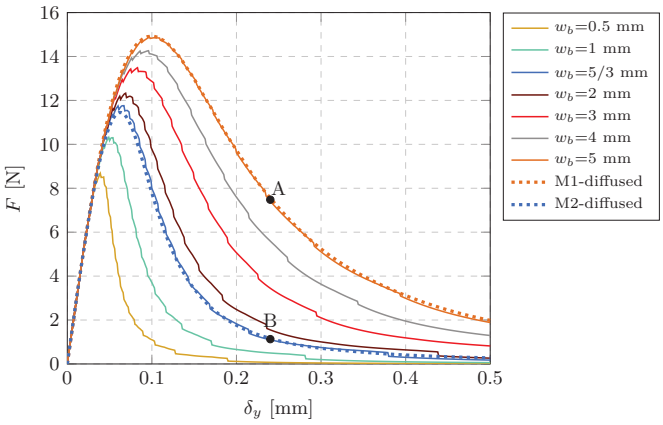

Figure 16: Example 2 - Load-displacement curves. Markers A and B indicate two states for which the deformed shapes are plotted in Figure 17.

5.3. Example 3: double edge notched specimen under tensile load

Another common test where crack opens in mode I is the tensile test on a double edge notched specimen. The peculiarity of this test lies in the propagation of two cracks which finally merge into one. The test is also chosen to compare our results with others available in the literature, in this case those obtained by Benvenuti et al. [41]. To this end, same geometry and material parameters as in [41] are adopted. Dimensions of the specimen are reported in Figure 18a, where the coarser mesh, external constraints and loading conditions are also visible. Figure 18b shows instead a second adopted denser mesh. The thickness of the specimen is 10 mm. Material parameters are in Table 6. All elements are quadrilateral and linear. The specimen is fixed at its base and loaded by imposing vertical incremental displacements until the

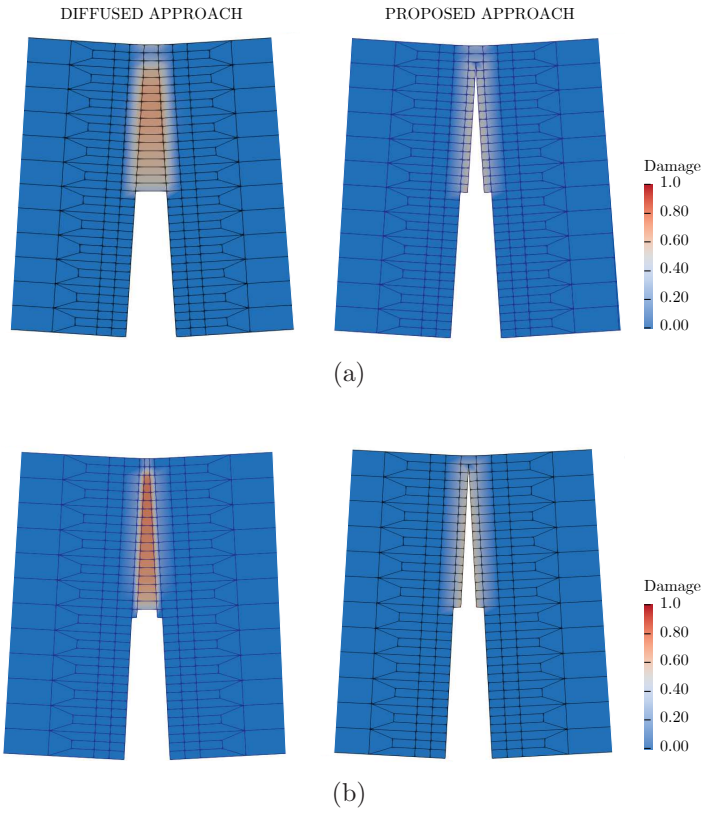

Figure 17: Example 2 - Damage maps and deformed shape comparison between the proposed approach (on the right) applied on M1 mesh and diffused approach for (a) M1 and (b) M2 meshes (on the left).

Table 6: Example 3 - Material parameters

$E\ [MPa]$	ν	ε_0	$\frac{\varepsilon_f}{\varepsilon_0}$	$w_b\ [mm]$	D_{crit}
2000	0.2	$5E-4$	500	1	0.55

final value $\bar{\delta}_y = 1\ mm$.
The load-displacement curves for the two meshes are plotted in Figure 19 together with the numerical result of the regularized X-FEM model in [41]. Since the interphase thickness is fixed to 1 mm and crack is perfectly horizontal, both coarse and dense meshes give the same mesh independent response. This response is also in very good agreement with ref. [41]. Strain localization takes place when the load-displacement curve attains its peak value. Two cracks form symmetrically at the two notches, propagate during the softening branch and meet halfway merging on the symmetry axis. Crack openings and damage patterns are reported, for the denser mesh, on the deformed shapes of Figure 20, corresponding to an imposed displacement multiplier of 0.104 (Fig. 20a), 0.116 (Fig. 20b), and 0.134 (Fig. 20c), respectively.

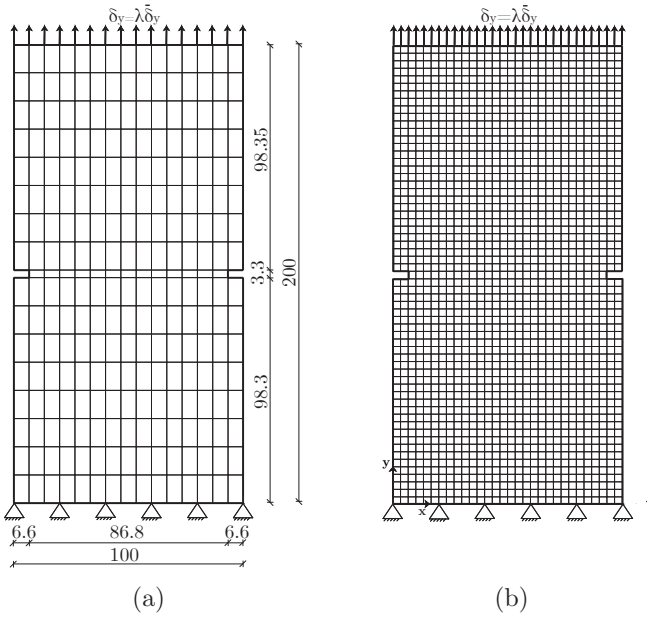

Figure 18: Example 3. Meshes and boundary conditions, with measures expressed in mm. (a) Coarse mesh, (b) Dense mesh.

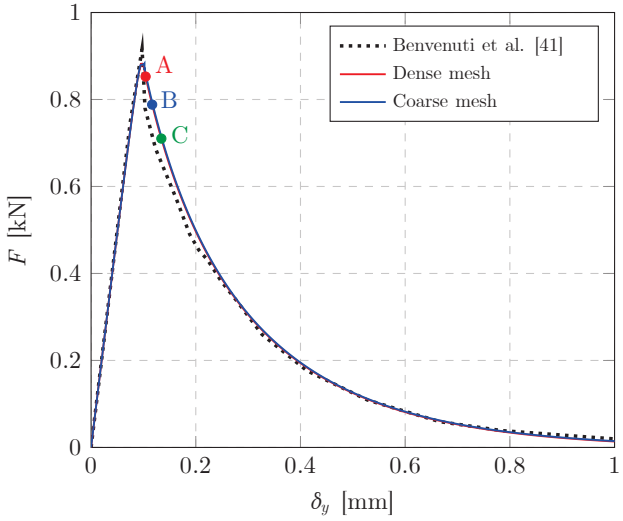

Figure 19: Example 3 - Load-displacement curves. Markers A, B, C indicate three states for which the deformed shapes are plotted in Figure 20.

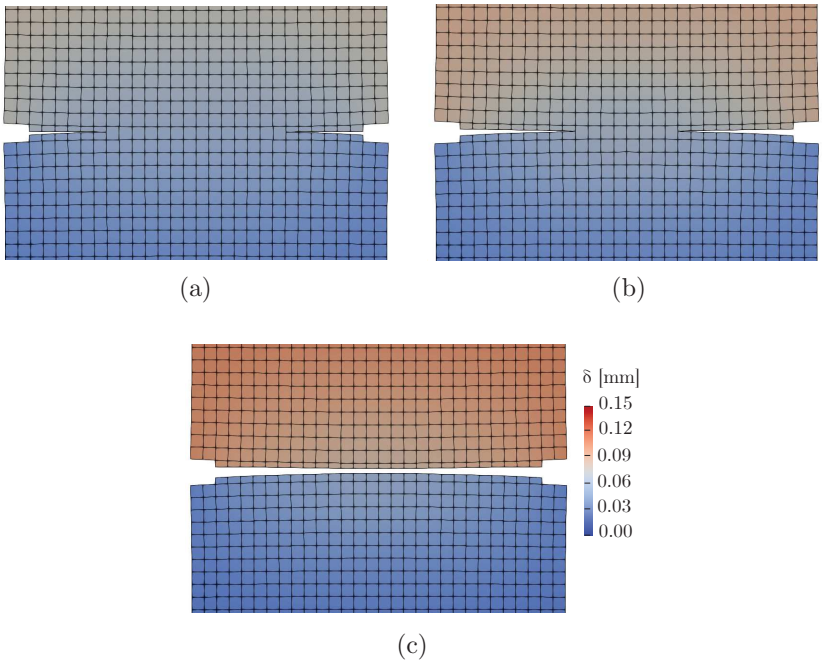

Figure 20: Example 3 - Crack evolution on deformed shape at steps (a) A, (b) B, (c) C of Figure 19.

Table 7: Example 4 - Material parameters

$E\ [MPa]$	ν	ε_0	$\frac{\varepsilon_f}{\varepsilon_0}$	$w_b\ [mm]$	D_{crit}
20000	0.2	$1.38E-4$	140	1	0.1

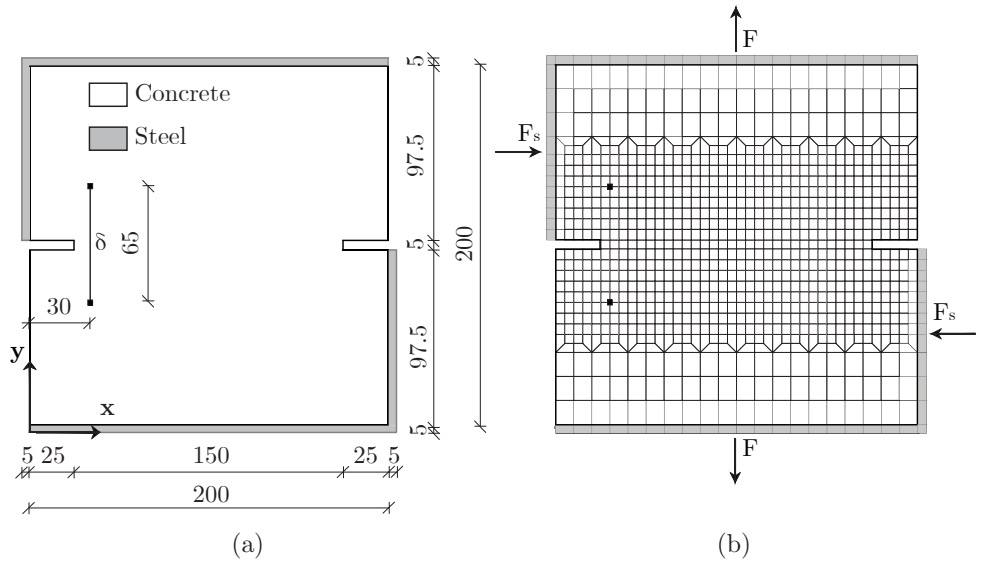

Figure 21: Example 4 - (a) Geometry and boundary conditions; (b) Numerical mesh. Measures are expressed in mm.

5.4. Example 4: double edge notched specimen under mixed mode

This new example is mainly guided by the intention of comparing numerical results with experimental data. The double edge notched concrete specimen analyzed by Nooru-Mohamed in 1993 [43], using a mixed-mode loading machine, is considered as a reference. This experimental machine consists of two independent stiff frames able to induce a combination of shear and tensile (or compressive) stress on the specimen. Among the different experimental tests conducted in [43], we simulate the loading paths '4*a*' and '4*b*', regarding a 200 *mm* square specimen with two symmetrical notches, as in Figure 21a. The two loading steel frames are experimentally glued to the specimen at its entire depth, equal to 50 *mm*.

Experimental load was applied in two phases. In the first phase the specimen was laterally pushed in displacement control until the resultant force F_s

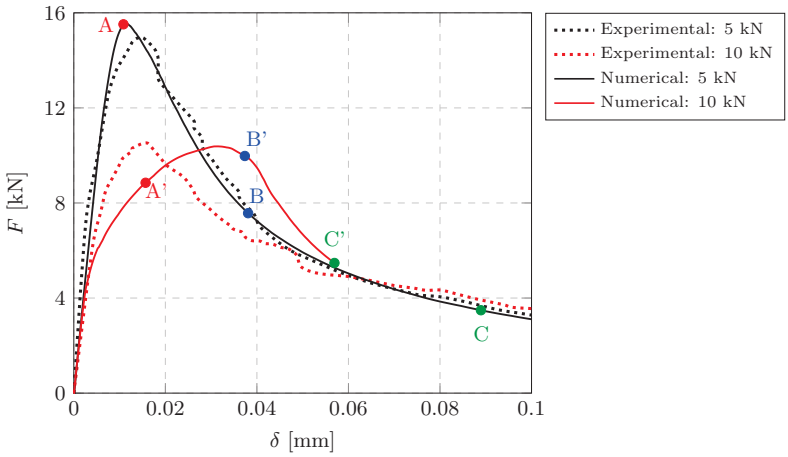

Figure 22: Example 4 - Load-displacement curves. Markers A, B, C indicate three states for which the deformed shapes are plotted in Figure 23. Markers A', B', C' indicate three states for which the deformed shapes are plotted in Figure 24.

reached the values of 5 kN and 10 kN for the paths 4a and 4b respectively. In the second phase, the horizontal F_s force was kept constant, while the test continued under incremental vertical displacement.

In [43] the experimental load-displacement curves are reported in terms of vertical resultant force F versus the relative vertical displacement δ between the two control points of Figure 21a. The resulting experimental curves are plotted in dotted lines in Figure 22. The observed damage pattern consisted of two curved cracks starting from the two notches with a steeper inclination the higher the F_s lateral force, and propagating in parallel. Nooru-Mohamed affirmed that, although the experimental machine was precise and sophisticated, undesirable eccentricities associated with the skew-symmetry of the test were observed. Such effects might result in experimental cracks that are not perfectly symmetric and could affect the load-displacement curves.

Numerical tests are run on the mesh showed in Figure 21b. This is composed of 910 initially quadrilateral linear elements, with a denser tessellation in the crack propagating area. In order to accurately reproduce the experimental loading phases, the elements representing the steel frames are first horizontally pushed under displacement control. The imposed displacements are calibrated so that F_s is exactly 5 kN or 10 kN. Once F_s attains its prescribed value, horizontal constraints are converted into external applied forces which are maintained constant throughout the rest of the test. During

this, the specimen is vertically stretched under displacement control. The vertical displacement δ reported in Figure 22 is the relative one between the two evaluation points marked in Figure 21b. Material parameters are those furnished by [44] and reported in Table 7. The localization and final strains reported in Table 7 are calibrated on the $F_s = 5\ kN$ case for an interphase thickness equal to 1 mm.

The experimental-numerical comparison in terms of load-displacement curves in Figure 22 shows a very close match in the 5 kN case, for which numerical parameters are calibrated. The 10 kN numerical curve, in addition,

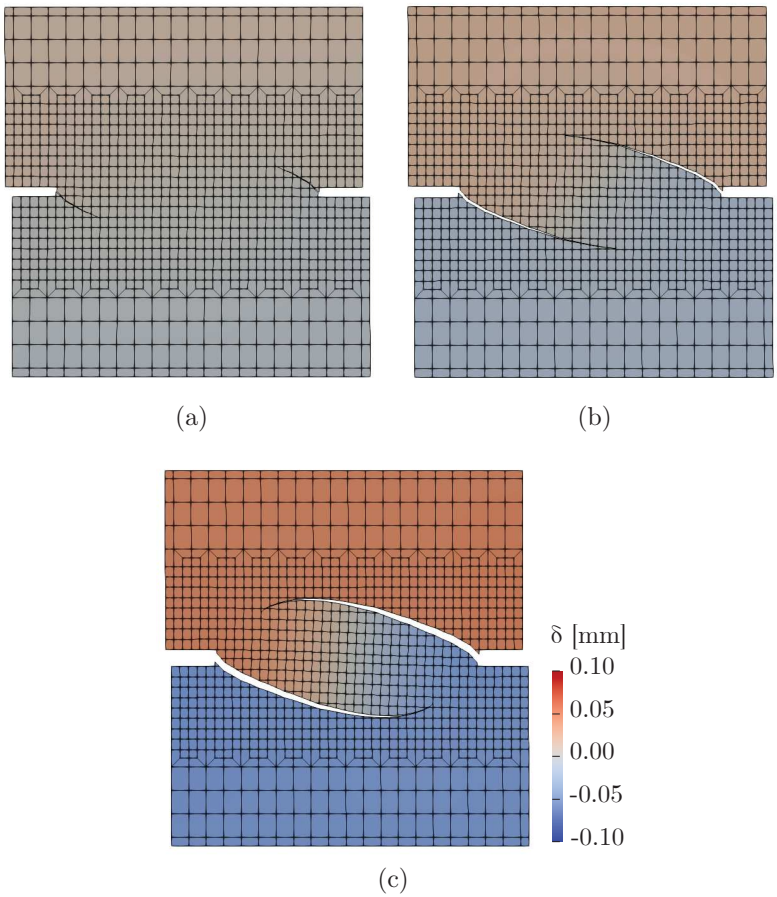

Figure 23: Example 4 - Crack evolution at steps (a) A, (b) B, (c) C of Figure 22, when $F = 5\ kN$.

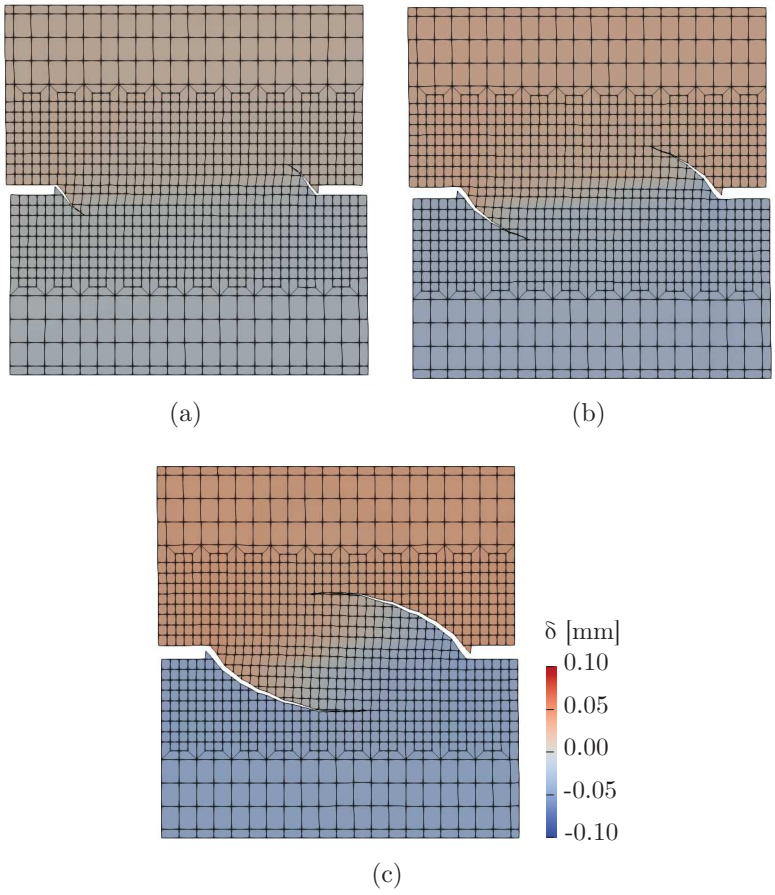

Figure 24: Example 4 - Crack evolution at steps (a) A', (b) B', (c) C' of Figure 22, when $F = 10\ kN$.

shows a peak equal to the experimental one, the same initial stiffness and a similar nonlinear trend. In contrast, when cracks begin to propagate, nonlinear behavior becomes more deformable. Regarding the numerical curve, this discrepancy could be possibly related to the value of interphase thickness adopted for both cases; regarding the experimental curve, it could be related to the declared undesired eccentricities.

Crack extension at A, B, and C marked points in Figure 22 is reported in Figure 23 for the $F_s = 5\ kN$ case. In an analogous fashion, Figure 24 shows the crack evolution for A', B', and C' marked points in Figure 22. Cracks

form and propagate symmetrically, as expected. As found experimentally, cracks evolving in the 5 kN case are more flattened than in the 10 kN case. Overall, a fairly good match is obtained when comparing numerical and experimental results.

In order to show the influence of internal stresses and strains on the overall mechanical response of the FE model, the $F_s = 5\ kN$ case is run neglecting the components of the stiffness matrix connected to the internal strains. Although the fracture process is governed by tensile tractions, the load-displacement response in the post-peak stage is lower (Fig. 25a). Not much difference is apparent in Figure 25b.

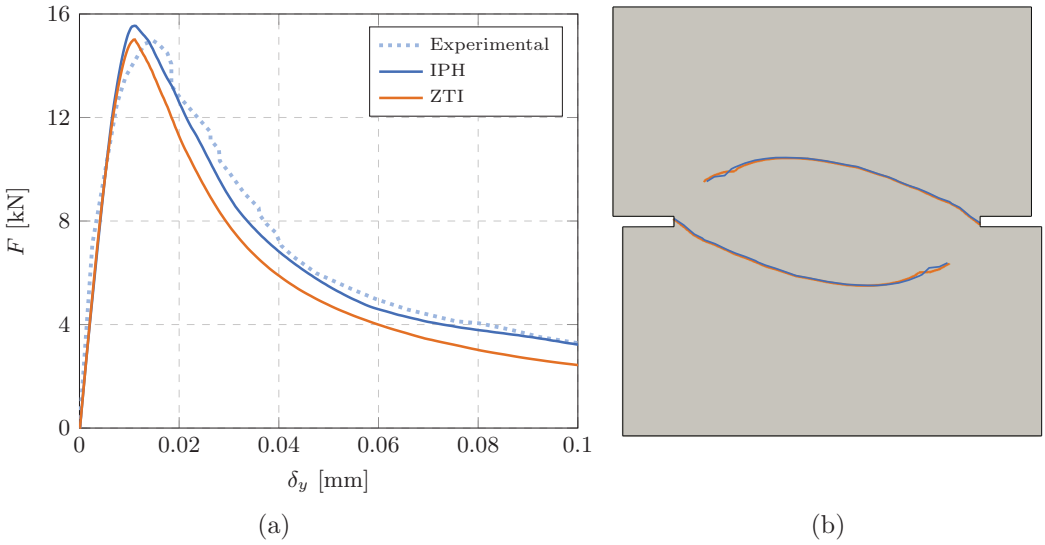

Figure 25: Example 4 - IPH/ZTI comparison: a) Load-displacement curves; b) crack patterns.

6. Conclusions

The present work deals with simulation of strain localization and fracture in structures made up of quasi-brittle material modelled in the framework of isotropic damage mechanics.

To simulate strain localization and its evolution in a pure crack, a numerical strategy integrated within the Finite Element Method combines the discrete crack approach and a crack tracking algorithm.

An advanced augmented finite element method (AAFEM) has been used to model the continuous-discontinuous transition, which differs from the classical formulation by introducing an interphase element instead of a zero-thickness interface. This advancement produces the following advantages:

- when strain localization occurs, according to localization theory, the interphase simulates weak discontinuity since the strain state in the thin layer is separated into regular and irregular parts (internal and contact strains), the latter of which suffers discontinuity. The ZTI models contact strain components only. When the damage value reaches the unit value, the interphase simulates the crack since there is no stress transfer and the displacement within the finite element is discontinuous. Therefore, the advantage of the method is the ability to follow the whole process from weak to strong discontinuities;

- it is no longer necessary to introduce a specific traction-discontinuous displacement constitutive law for the localization band, because the interphase is a solid with simplified kinematics which has the same constitutive behavior as the bulk material. Furthermore, the number of constitutive parameters is also reduced. Only the band thickness w_b needs to be added to the bulk material parameters.

In relation to the second point, it is noteworthy that two questions arise when using classical AFEM. The first is: what constitutive model and what related mechanical parameters should be assigned to the interface in some way consistent with the constitutive material model that governs the process of diffuse damage prior to localization? The second question is: What are the values of the internal variables that characterize the response of the interface when the continuous-discontinuous transition is activated?
The proposed approach overcomes the aforementioned issues because the quasi-brittle material pre- and post- strain localization have the same constitutive model. Moreover, at the transition stage, the values of the internal variables are evaluated on the basis of the values attained by the same variables in the material surrounding the band.
The localization band or crack tracking procedure is another important aspect of the study. It includes the evaluation of the position and direction of each discontinuity in the finite element and the definition of its propagation from one element to another.
The algorithm here proposed presents some original aspects:

- the localization band is inserted into the finite element on the basis of a double criterion, namely when the minimum eigenvalue of the tangential stiffness matrix of the element becomes zero or negative and at the same time the damage variable reaches the critical value. The critical damage is an additional constitutive parameter whose value should not necessarily be close to unity, as is the case in other works in the literature. This is because it serves to trigger the localization before the pure crack and not the crack itself;

- the interphase line is positioned in the element using a point and a direction. The point is the balance point of the damage values evaluated at the Gauss sample points. The direction is obtained by spectral decomposition of the localization tensor of the element. The localization tensor, introduced here, weighs the directions of the maximum principal strain at the Gauss points by the damage values associated with the same points;

- a clustering technique groups the elements of the model potentially crossed by the localization band or fracture. Each group is converted into substructures that are numerically analyzed separately to find the nonlinear response at each time step. The transformation of clusters into substructures consists in selecting the elements to which the localization band actually belongs. This selection is based on simple heuristic criteria.

The proposed numerical strategy was applied to some two-dimensional tests, and the results were compared with the same tests whose solution is reported in the literature and with available experimental results. These results are encouraging, since:

- the numerical responses, in terms of load-displacement curves and fracture patterns, agree with the results reported in the literature and they are independent of mesh size and mesh bias;

- the convergence at the sub-structure level and at the overall level is acceptable (mostly quadratic).

Currently, the numerical strategy does not take into account crack branching in the element and crack propagation between two adjacent elements (interelement crack). Therefore, these two aspects are the subject of future

work.
Since the method presented is general, the authors assume that it can be readily applied to elastoplasticity for materials that exhibit strain-softening and are particularly subjected to strain localization.
For instance, in soil mechanics, collapse mechanisms are dominated by the formation of shear bands. The method can be used to simulate relevant engineering problems such as soil-foundation interaction and slope stability.

7. Acknowledgments

A. Spada acknowledges the financial support of the project FFR2021-D26-SPADA - Fondo di Finanziamento per la Ricerca di Ateneo.
G. Giambanco acknowledges the financial support of the project FFR2021-D26-GIAMBANCO - Fondo di Finanziamento per la Ricerca di Ateneo.

References

[1] J. W. Rudnicki, J. Rice, Conditions for the localization of deformation in pressure-sensitive dilatant materials, J. Mech. Phys. Solids 23 (1975) 371–394.

[2] N. Ottosen, K. Runesson, Properties of discontinuous bifurcation solutions in elasto-plasticity, Int. J. Solids Struct. 27 (1991) 401–421.

[3] T. Belytschko, J. Fish, B. E. Engelmann, A finite element with embedded localization zones, Comput. Methods Appl. Mech. Eng. 70 (1988) 59–89.

[4] L. J. Sluys, A. H. Berends, Discontinuous failure analysis for mode-I and mode-II localization problems, Int. J. Solids Struct. 35 (1998) 4257–4274.

[5] J. C. Simo, J. Oliver, F. Armero, An analysis of strong discontinuity induced by strain-softening in rate-independent inelastic solids, Comput. Mech. 12 (1993) 277–296.

[6] J. Oliver, Modelling strong discontinuities in solid mechanics via strain softening constitutive equations. Part 1: Fundamentals. Part 2: Numerical Simulation, Int. J. Numer. Methods Eng. 39 (1996) 3575–3624.

[7] E. Sacco, F. Lebon, A damage-friction interface model derived from micromechanical approach, Int. J. Solids Struct. 49 (26) (2012) 3666–3680.

[8] C. Polizzotto, Unified thermodynamic framework for nonlocal/gradient continuum theories, Eur. J. Mech. A Solids 22 (2003) 651–668.

[9] E. C. Aifantis, Update on a class of gradient theories, Mech. Mater. 35 (2003) 259–280.

[10] F. Freddi, G. Royer Carfagni, Phase-field slip-line theory of plasticity, J. Mech. Phys. Solids 94 (2016) 257–272.

[11] G. Giambanco, E. La Malfa Ribolla, A phase-field model for strain localization analysis in softening elastoplastic materials, Int. J. Solids Struct. 172-173 (2019) 84–96.

[12] P. Areias, T. Rabczuk, Finite strain fracture of plates and shells with configurational forces and edge rotations, Int J Numer Methods Eng 94 (2013) 1099–1122.

[13] X. P. Xu, A. Needleman, Numerical simulations of fast crack growth in brittle solids, J. Mech. Phys Solids 42 (1994) 1397–1434.

[14] G. T. Camacho, M. Ortiz, Computational modelling of impact damage in brittle materials, Int. J. Solids Struct. 33 (1996) 2899–2938.

[15] T.-P. Fries, T. Belytschko, The extended/generalized finite element method: an overview of the method and its applications, Int. J. Numer. Methods Eng. 84 (2010) 253–304.

[16] N. Moës, T. Belytschko, Extended finite element method for cohesive crack growth, Eng. Fract. Mech. 69 (2002) 813–833.

[17] I. Babuška, G. Caloz, J. Osborn, Special finite element methods in a class of second order elliptic problems with rough coefficients, SIAM J. Numer. Anal. 31 (1994) 945–981.

[18] M. Cervera, G. Barbat, M. Chiumenti, J. Wu, A comparative review of xfem, mixed fem and phase-field models for quasi-brittle cracking, Archives of Computational Methods in Engineering 29 (2022) 1009–1083.

[19] A. Hansbo, P. Hansbo, A finite element method for the simulation of strong and weak discontinuities in solid mechanics, Comput. Methods Appl. Mech. Eng. 193 (2004) 3523–3540.

[20] G.-H. Song, P. Areias, T. Belytschko, A method for dynamic crack and shear band propagation with phantom nodes, Int. J. Numer. Methods Eng. 67 (2006) 868–893.

[21] T. Rabczuk, G. Zi, A. Gerstenberger, W. A. Wall, A new crack tip element for the phantom-node method with arbitrary cohesive cracks, Int. J. Numer. Methods Eng. 75 (2008) 577–599.

[22] E. Artioli, S. Marfia, E. Sacco, Vem-based tracking algorithm for cohesive/frictional 2d fracture, Comput. Methods Appl. Mech. Eng. 365 (2020) 112956.

[23] T. Rabczuk, T. Belytschko, Cracking particles: a simplified meshfree method for arbitrary evolving cracks, Int J Numer Methods Eng 61 (2004) 2316–2343.

[24] Y. Zhang, X. Zhuang, Cracking elements: a self-propagating strong discontinuity embedded approach for quasi-brittle fracture, Finite Elements in Analysis and Design 144 (2018) 84–100.

[25] D. Ling, Q. Yang, B. Cox, An augmented finite element method for modeling arbitrary discontinuities in composite materials, Int. J. Fract. 156 (2009) 53–73.

[26] W. Liu, Q. Yang, S. Mohammadizadeh, X. Su, An efficient augmented finite element method for arbitrary cracking and crack interactions in solids, Int. J. Numer. Methods Eng. 80 (2013).

[27] S. Essongue, G. Couégnat, E. Martin, Performance assessment of the augmented finite element method for the modeling of weak discontinuities, Int J Numer Methods Eng 122 (2021) 172–189.

[28] Z. Ma, Q. Yang, X. Su, A conforming augmented finite element method for modeling arbitrary cracking in solids, Journal of Applied Mechanics 86 (2019) 071002.

[29] G. Giambanco, Z. Mróz, The interphase model for the analysis of joints in rock masses and masonry structures, Meccanica 36 (2001) 111–130.

[30] G. Giambanco, G. F. Scimemi, A. Spada, The interphase finite element, Comput. Mech. 50 (2012) 353–366.

[31] M. Jirásek, Damage and smeared crack models, in: Numerical modeling of concrete cracking, Springer, 2011, pp. 1–49.

[32] M. Jirásek, T. Zimmermann, Embedded crack model: I. Basic formulation, Int. J. Numer. Methods Eng. 50 (2001) 1269–1290.

[33] M. Jirásek, T. Zimmermann, Embedded crack model. Part II: Combination with smeared cracks, I 50 (2001) 1291–1305.

[34] G. Borré, G. Maier, On linear versus nonlinear flow rules in strain localization analysis, Meccanica 24 (1989) 36–41.

[35] E. Rizzi, I. Carol, K. Willam, Localization analysis of elastic degradation with application to scalar damage, J. Eng. Mech. 121 (1995) 541–554.

[36] C. Comi, S. Mariani, U. Perego, An extended FE strategy for transition from continuum damage to mode I cohesive crack propagation, Int. J. Numer. Anal. Meth. Geomech. 31 (2007) 213–238.

[37] E. Tamayo-Mas, A. Rodríguez-Ferran, A medial-axis-based model for propagating cracks in a regularised bulk, Int. J. Numer. Methods Eng. 101 (2015) 489–520.

[38] Y. Wang, H. Waisman, From diffuse damage to sharp cohesive cracks: a coupled xfem framework for failure analysis of quasi-brittle materials, Comput. Methods Appl. Mech. Eng. 299 (2016) 57–89.

[39] M. Jirásek, T. Zimmermann, Rotating crack model with transition to scalar damage, J. Eng. Mech. 124 (1998) 277–284.

[40] A. Munjiza, K. Andrews, Nbs contact detection algorithm for bodies of similar size, Int. J. Numer. Methods Eng. 43 (1998) 131–149.

[41] E. Benvenuti, N. Orlando, A mesh-independent framework for crack tracking in elastodamaging materials through the regularized extended finite element method, Comput. Mech. (2021) 1–25.

[42] S. Saloustros, M. Cervera, L. Pelà, Challenges, tools and applications of tracking algorithms in the numerical modelling of cracks in concrete and masonry structures, Arch. Comput. Methods Eng. 26 (2019) 961–1005.

[43] M. B. Nooru-Mohamed, Mixed-mode fracture of concrete: An experimental approach., Ph.D. thesis, Technische Universiteit Delft (The Netherlands), 1993.

[44] B. Patzák, M. Jirásek, Adaptive resolution of localized damage in quasi-brittle materials, J. Eng. Mech. 130 (2004) 720–732.